

VISIBLE AND NEAR INFRARED EMITTING THIN FILM  
ELECTROLUMINESCENT GALLIUM NITRIDE DOPED WITH RARE EARTHS

By

JOO HAN KIM

A DISSERTATION PRESENTED TO THE GRADUATE SCHOOL  
OF THE UNIVERSITY OF FLORIDA IN PARTIAL FULFILLMENT  
OF THE REQUIREMENTS FOR THE DEGREE OF  
DOCTOR OF PHILOSOPHY

UNIVERSITY OF FLORIDA

2003

This dissertation is dedicated to my family for their loving support and continuing encouragement, especially my father and mother and my wife and two sons, who have always believed in me and my dreams.

## ACKNOWLEDGMENTS

First of all, it is a great pleasure to thank my advisor, Dr. Paul H. Holloway, for his patient attention and wise advice. He always paid close attention to my interests and he was a model advisor for my dissertation work. His knowledge and expertise were invaluable in the course of my studies and I feel fortunate to have worked with him. It is also my great honor to have four other distinguished professors, Dr. Stephen J. Pearton, Dr. Timothy Anderson, Dr. Wolfgang Sigmund, and Dr. Rajiv Singh, as my committee members.

I would like to thank Ms. Ludie Harmon for her lovely smile and keeping things going smoothly. I want to thank the staff of the Microfabritech for their continued assistance throughout my stay at Microfabritech. Special thanks go to Dr. Mark Davidson, Mr. Chuck Rowland, Mr. Scott Gapinsk, Ms. Diane Badylak, Joyce, Andre, and Jim. For help with sample analyses, I am especially grateful to Mr. Eric Lambers for AES and XPS, Dr. Valentin Craciun for XRD, Mr. Wayne Acree and Dr. Amelia Dempere for SEM and EPMA analyses. I want to thank everyone in Dr. Holloway's lab for providing me with a positive study environment. Special thanks go to Jay Lewis and David Moorehead, who both have been cooperative to me. Thanks go also to all the people in the UF MSE department who supported and helped me to prepare this work.

Finally, I am immeasurably indebted to my father and mother in Korea, who have always believed in me and my dreams. They taught me what the true love is. I am also greatly indebted to my lovely wife, Hyewon, who has shown me a warm heart and

supported me all the time. Thanks go to our precious two children, Yoonjae and Seungjae, who both were born during this journey. I want everyone in my family to know that I sincerely appreciate all of their loving support and encouragement. I could never have finished this work without their endless love and support. I am very glad to say to them that I am finally through the tunnel.

## TABLE OF CONTENTS

	<u>page</u>
ACKNOWLEDGEMENTS .....	iii
LIST OF TABLES .....	viii
LIST OF FIGURES .....	ix
ABSTRACT.....	xii
 CHAPTERS	
1 INTRODUCTION .....	1
2 LITERATURE REVIEW .....	4
2.1 Introduction.....	4
2.2 ACTFEL Device Structures.....	5
2.3 ACTFEL Device Physics.....	6
2.4 ACTFEL Device Materials.....	7
2.4.1 Substrate.....	7
2.4.2 Transparent Conducting Electrode.....	7
2.4.3 Dielectrics .....	8
2.4.4 ACTFEL Phosphors.....	8
2.5 Rare-Earth Luminescent Centers .....	10
2.6 Sulfide-based EL Phosphors.....	12
2.7 III-Nitride-based EL Phosphors.....	14
2.7.1 Gallium Nitride Host.....	16
2.7.4 Rare Earth Activators in Gallium Nitride .....	17
3 EXPERIMENTAL PROCEDURES .....	25
3.1 Gallium Nitride Thin Film Deposition .....	25
3.2 Rare-earth-doped GaN ACTFEL Device Fabrication .....	26
3.3 Rare-earth-doped GaN Heat Treatment .....	27
3.4 Characterizations.....	28
3.4.1 Structure and Composition Analyses.....	29
3.4.2 Photoluminescence and Electroluminescence Characterizations .....	31
3.4.3 Electrical Characterizations .....	33

4	STRUCTURE AND PROPERTIES OF GALLIUM NITRIDE THIN FILMS .....	40
4.1	Introduction.....	40
4.2	Experimental Results .....	42
4.2.1	Phase Transition in GaN Thin Films .....	42
4.2.2	Internal Stress of GaN Thin Films .....	44
4.2.3	Microstructure Evolution of GaN Thin Films .....	45
4.3	Discussion .....	46
4.3	Summary .....	49
5	TEXTURED GROWTH OF CUBIC GALLIUM NITRIDE THIN FILMS.....	58
5.1	Introduction.....	58
5.2	Experimental Results and Discussion.....	59
5.2.1	Growth Rate of Cubic GaN Thin Films .....	59
5.2.2	X-ray Diffraction and Pole Figures.....	59
5.2.2	X-ray Rocking Curves of Cubic GaN Thin Films .....	61
5.2.2	Auger Electron Spectroscopy Analysis .....	62
5.3	Summary .....	63
6	PHOTOLUMINESCENCE AND ELECTROLUMINESCENCE OF EUROPIUM-DOPED GALLIUM NITRIDE.....	72
6.1	Introduction.....	72
6.2	Experimental Results and Discussion.....	73
6.2.1	X-ray Photoelectron Spectroscopy Analysis .....	73
6.2.2	Photoluminescence Study.....	74
6.2.3	Electroluminescence Characteristics .....	75
6.3	Summary .....	77
7	ELECTROLUMINESCENCE OF THULMIUM-DOPED GALLIUM NITRIDE .....	84
7.1	Introduction.....	84
7.2	Experimental Results and Discussion.....	85
7.2.1	Electroluminescence Emission Spectra .....	85
7.2.2	Emission Intensity versus Voltage Curves .....	86
7.2.3	Electroluminescence Excitation Mechanisms.....	87
7.3	Summary .....	89
8	ELECTROLUMINESCENT CHARACTERISTICS AND STRUCTURAL PROPERTIES OF ERBIUM-DOPED GALLIUM NITRIDE .....	95
8.1	Introduction.....	95
8.2	Experimental Results and Discussions .....	97
8.2.1	Crystalline Structure of Er-doped GaN.....	97
8.2.2	Visible and Near-Infrared Electroluminescence.....	98
8.2.3	Emission Intensity versus Voltage Analysis.....	100

8.3 Summary .....	101
9 NEAR-INFRARED ELECTROLUMINESCENCE FROM NEODYMIUM-DOPED GALLIUM NITRIDE .....	110
9.1 Introduction.....	110
9.2 Experimental Results and Discussions .....	111
9.2.1 X-ray Diffraction Analysis .....	111
9.2.2 Near-Infrared Electroluminescent Emission from Nd-doped GaN .....	112
9.2.3 Visible Electroluminescent Emission from Nd-doped GaN.....	113
9.2.4 Excitation Mechanisms.....	113
9.3 Summary.....	114
10 CONCLUSIONS.....	120
11 FUTURE WORK.....	123
LIST OF REFERENCES.....	125
BIOGRAPHICAL SKETCH .....	129

## LIST OF TABLES

<u>Table</u>	<u>Page</u>
2-1 Thin-film insulating materials typically used in ACTFEL devices .....	9
2-2 The lanthanide series .....	11
2-3 Physical properties of GaN .....	18
3-1 Sputter deposition parameters of GaN thin films doped with rare earths.....	27



## LIST OF FIGURES

<u>Figure</u>	<u>Page</u>
2-1 Performance of TFELDs in comparison with competing LCDs (a) temperature range, (b) viewing angle, (c) response time .....	19
2-2 Conventional structure of a double-insulating-layer type ACTFEL device .....	20
2-3 Energy band diagram of the double-insulating-layer type ACTFEL device and the EL emission mechanism .....	21
2-4 Energy band levels of the $4f^n$ configurations of the trivalent lanthanide ions .....	22
2-5 Square of the radial wave functions of Gd atom showing that the 4f electron orbital lies well inside the outer filled 5s and 5p orbitals .....	23
2-6 Partial energy diagrams of trivalent rare earth ions of Eu, Tm, Er, and Nd .....	24
3-1 Schematic illustration of the radio frequency (RF) planar magnetron sputtering system.....	35
3-2 Structure of half-stack ACTFEL devices based on rare earth-doped GaN systems.....	36
3-3 Schematic of brightness versus voltage curve .....	37
3-4 CIE 1931 chromaticity diagram.....	38
3-5 Q-V characteristics of an ACTFEL device.....	39
4-1 X-ray diffraction patterns of the GaN films grown on Si (100)-oriented substrates at various nitrogen gas pressures .....	51
4-2 X-ray diffraction patterns of the GaN films grown on Si (111)-oriented substrates at various nitrogen gas pressures .....	52
4-3 Peak deconvolution of the hexagonal wurtzite (0002) and cubic zinc-blende (111) Bragg diffraction peaks .....	53
4-4 Variation in the XRD intensity ratio of the zinc-blende (111) to wurtzite (0002) peak as a function of the nitrogen gas pressure during film growth .....	54
4-5 Dependence of the internal stress in the GaN films on the nitrogen gas pressure.....	55

4-6 Cross-sectional field-emission scanning electron micrographs of the GaN films grown on Si (111) substrates .....	56
4-7 Variation in the XRD peak intensity ratio of $I_{ZB(111)}/I_{W(0002)}$ as a function of the average compressive stress in the films.....	57
5-1 Dependence of the growth rate of cubic GaN films on the RF power applied to the GaN cathode target .....	65
5-2 X-ray diffraction $\theta$ - $2\theta$ scans for the cubic GaN films grown at different RF cathode target powers.....	66
5-3 Internal stress in the GaN films as a function of the RF power applied to the GaN cathode target.....	67
5-4 X-ray pole figure obtained from the GaN films grown at a RF cathode target power of 10 W.....	68
5-5 X-ray rocking curves for the (111) diffraction peak collected from the GaN films grown at various RF cathode target powers .....	69
5-6 Auger electron spectra collected from the GaN films grown at various RF cathode target powers.....	70
5-7 Auger depth profiles collected from the GaN films grown at various RF cathode target powers.....	71
6-1 XPS spectrum of the Eu 4 <i>d</i> core level collected for Eu-doped GaN films.....	78
6-2 Photoluminescence (PL) spectrum recorded at room temperature from Eu-doped GaN films.....	79
6-3 Partial energy level diagram for an $\text{Eu}^{3+}$ ion .....	80
6-4 Dependence of the intensity of 614 nm photoluminescence emission peak on the concentration of Eu in GaN host films .....	81
6-5 Electroluminescence (EL) spectrum emitted from Eu-doped GaN films.....	82
6-6 EL intensity versus applied AC peak voltage ( <i>I-V</i> ) data .....	83
7-1 Alternating-current electroluminescent spectrum collected from a SD GaN:Tm ACTFEL device.....	90
7-2 Simplified energy level diagram for a $\text{Tm}^{3+}$ ion.....	91
7-3 EL emission intensity versus applied AC peak voltage ( <i>I-V</i> ) curves .....	92
7-4 Dependence of the EL intensity ratio of 475 nm to 800 nm emission, $I_{475}/I_{800}$ , on the	

AC voltage applied to the devices .....	93
7-5 Plots of logarithm of the EL emission intensity, $\ln(I)$ , versus the reciprocal square root of the applied AC voltage, $V^{-1/2}$ , for blue 475 nm and NIR 800 nm emission peaks.....	94
8-1 X-ray diffraction patterns obtained from Er-doped GaN films with the variation of Er concentration .....	103
8-2 Variation in (a) $c$ lattice constant of wurtzite GaN and (b) full width at half maximum (FWHM) of the (0002) wurtzite GaN peak as a function of Er concentration.....	104
8-3 A typical room temperature visible spectrum emitted from the sputter-grown GaN:Er ACTFEL devices .....	105
8-4 Energy level diagram for $\text{Er}^{3+}$ ion.....	106
8-5 A typical room temperature near-infrared (NIR) spectrum emitted from the sputter-grown GaN:Er ACTFEL devices .....	107
8-6 EL intensity versus applied AC peak voltage ( $I$ - $V$ ) data .....	108
8-7 Variation in the (a) near-infrared 1550 nm and (b) visible 530 nm EL emission intensity as a function of Er concentration .....	109
9-1 X-ray diffraction patterns collected from (a) undoped GaN and (b) ~1.2 at.% Nd-doped GaN films.....	115
9-2 Near-infrared electroluminescence spectra emitted from Nd-doped GaN EL devices ..	116
9-3 Optical transition level diagram of the trivalent Nd ion.....	117
9-4 Visible electroluminescence emission spectrum emitted from Nd-doped GaN EL devices.....	118
9-5 EL intensity versus applied AC peak voltage ( $I$ - $V$ ) curves.....	119

Abstract of Dissertation Presented to the Graduate School  
of the University of Florida in Partial Fulfillment of the  
Requirements for the Degree of Doctor of Philosophy

VISIBLE AND NEAR INFRARED EMITTING THIN FILM  
ELECTROLUMINESCENT GALLIUM NITRIDE DOPED WITH RARE EARTHS

By Joo Han Kim

December 2003

Chairman: Paul H. Holloway

Major Department: Materials Science and Engineering

Visible and near-infrared (NIR) light-emitting thin-film electroluminescent gallium nitride (GaN) doped with rare earth (RE) elements was studied. The rare-earth-doped GaN thin films were prepared by radio frequency (RF) planar magnetron co-sputtering of separate targets consisting of a GaN compound target and a metallic rare earth target in a pure nitrogen atmosphere.

The luminescence of rare-earth-doped GaN was shown to be a strong function of its structure and properties, and growth parameters affected the structure and properties of the GaN host films. A phase transition from the thermodynamically stable wurtzite to the metastable zinc-blende structure at room temperature in GaN host films was observed upon increasing the impact energy of the bombarding species, thereby increasing the compressive stress in the GaN film. The switch from wurtzite to zinc-blende GaN occurred at a compressive internal stress of  $\sim 1$  GPa. The internal compressive stress above this threshold value apparently stabilizes the zinc-blende GaN phase at room temperature. Field emission scanning electron microscopy (FESEM) and atomic force

microscopy (AFM) showed that the impact by hyperthermal species yielded a highly condensed fibrous GaN microstructure with a smooth surface morphology due to annihilation of porosity by knock-on and bombardment-induced adatom mobility.

X-ray diffraction and texture analyses showed that the GaN films deposited at a low pressure had a predominant cubic phase with a preferred crystallographic orientation of the [111] direction perpendicular to the surface of the film. X-ray rocking curve data revealed that cubic GaN films grown with a lower growth rate exhibited a more highly [111]-textured structure.

Alternating-current thin-film electroluminescent (ACTFEL) devices were fabricated based on GaN doped with rare earth (RE) elements. Visible electroluminescent light emission peaks at 475 (blue), 530 (green), and 614 nm (red) were demonstrated at room temperature from GaN doped with thulium (Tm), erbium (Er), and europium (Eu), respectively. The near-infrared electroluminescent light emissions at 800, 1082, and 1550 nm were obtained at room temperature from GaN doped with Tm, neodymium (Nd), and Er, respectively. The emitted power densities of the fabricated ACTFEL devices were  $\sim 1.53$ , 0.71, and  $3.48 \mu\text{W}/\text{cm}^2$  for the GaN doped with  $\sim 1$  at.% of Er,  $\sim 1.5$  at.% of Tm, and  $\sim 1.2$  at.% of Nd, respectively. The dominant electroluminescence excitation mechanism for RE-doped GaN was found to be direct impact-excitation of the trivalent RE ions by hot electrons.

## CHAPTER 1 INTRODUCTION

Presently, liquid crystal displays (LCDs) are popularly used in the area of flat panel displays (FPDs) [1]. However, they have many drawbacks such as poor characteristics under low temperature operation, reliance on viewing angle, and necessity of external light [2]. A great deal of research over the past decades has focused on alternative flat panel display technologies to LCDs which include thin film electroluminescent displays (TFELDs), field emission displays (FEDs), plasma panel displays (PDPs), and organic light emitting diodes (OLEDs). Among them, TFELDs have been considered as one of the most promising flat-panel displays to compete with LCDs because they offer a number of attractive advantages over LCDs [1]. These advantages include emissive display, completely solid state, wide viewing angles, wide operating temperatures, and fast response time [3]. In addition, they are extremely rugged and lightweight, and can operate under harsh environments, and thus, TFELDs are ideal for use in a wide variety of mobile applications [4].

Owing to these unique features, TFELDs have progressed from the commercialization of monochromatic flat panel displays in the early 80s (in 1983) to the development of multi-color and full-color displays in the 90s [1]. Sulfide-based ACTFEL phosphors, particularly ZnS, SrS, and  $\text{CaGa}_2\text{S}_4$ , have been typically studied for use in full-color ACTFEL display devices [5]. However, sulfide-based phosphors have intrinsic problems such as chemical instability and sensitivity to moisture, which make it difficult to pattern the phosphors by chemical etching or photolithography. In addition, sulfide-

based ACTFEL devices degrade within a short time when operated in the atmosphere owing to their chemical instability, particularly in regard to moisture. As a result, at present, long-term operation of ZnS phosphor TFEL devices has only been achieved by both the application of a double-insulating-layer structure and the use of a suitable device-sealing technique.

In the past few years, newer III-nitride-based phosphors have received an increasing amount of attention due to their unique properties such as higher chemical and thermal stability than sulfide phosphors [6]. In addition, III-nitrides, such as GaN and AlN are reported to be a promising phosphor host material for use in the full-color flat-panel thin-film electroluminescent display devices since they have a large enough bandgap to emit visible light from the luminescent center without significant absorption, and moreover, they were found to allow large concentrations of RE dopants without severe quenching of light emission [7]. Also, III-nitrides possess the ability to incorporate the trivalent RE ions without generating defects to maintain the charge neutrality, and thus, charge compensators, which are normally used in ZnS:RE<sup>3+</sup> phosphors to avoid crystal defects, are not needed in III-V nitrides:RE<sup>3+</sup> phosphors. It is, therefore, the goal of this work to develop the thin-film electroluminescent devices based on III-nitrides, particularly GaN, doped with RE impurities.

Besides the visible EL emission, near-infrared (NIR) electroluminescent light-emission from RE-doped GaN has in recent years been of great interest [6]. NIR light-emitting optical sources have a number of potential applications including friend/foe identifications in military action, night-vision illumination sources, chemical and biological sensing, consumer electronics, phototherapy, and spectroscopic analysis. In

particular, NIR emitters are essential ingredients in optical telecommunication systems. This is because the NIR light at the wavelengths of 0.8, 1.3, and 1.5  $\mu\text{m}$  coincides well with the wavelength of the minima in transmission loss and dispersion within the standard silica-based optical fibers [8]. In the present study, NIR light-emitting thin-film EL devices based on GaN doped with erbium (Er), thulium (Tm), and neodymium (Nd) have been developed.



## CHAPTER 2 LITERATURE REVIEW

### 2.1 Introduction

Cathode ray tubes (CRTs) have been widely used for information display applications since the first mass public demonstration of television occurred at the New York World's Fair in April 1939 [1]. The quest for a thin, flat, and lightweight replacement for the conventional CRTs, however, opened the door for the newer flat panel displays (FPDs). FPD technologies are being developed quite rapidly and they are replacing the conventional CRTs in many industrial and consumer product applications.

The term flat panel display unites all the non-CRT-type direct-view-displays. The FPDs can further be divided into two classes, liquid crystal displays (LCDs) and emissive displays. Presently, LCDs are popularly used and hold almost 90% of the market for small flat panel displays (< 14"). LCDs, however, have many drawbacks such as poor characteristics under low temperature operation, reliance on viewing angle, and necessity of external light [2]. The emissive FPDs include thin film electroluminescent displays (TFELDs), field emission displays (FEDs), plasma panel displays (PDPs), vacuum fluorescent displays (VFDs), organic and inorganic light-emitting diodes (LEDs). While each of these technologies has various advantages over the others, TFELDs have been considered as one of the most promising flat-panel displays to compete with LCDs because they offer a number of advantages over LCDs [9]. These advantages include excellent viewing properties and nearly constant luminance output over a wide temperature range, as illustrated in figure 3-1. And also, TFELDs offer fast response

times enabling rapid scrolling and cursor motion with no flicker or ghosting. In addition, their intrinsic ruggedness and resistance to harsh environments which result from their solid state nature make small to medium sized (2.5–20 cm in diagonal) TFELDs ideal for a wide variety of mobile applications [3]. These applications include mobile military systems, portable medical equipment, test and measurement instruments, etc.

For further information, refer to previous review articles presented by Rack *et al.*, [3] and Mach *et al.* [9] For the purpose of this study, a brief overview of the conventional ACTFEL device structure, device physics, and materials requirements is given. And also rare earth (RE) activators used in TFEL phosphors are discussed, followed by a summary of previous works related to sulfide-based and III-V nitride-based TFEL phosphors.

## 2.2 ACTFEL Device Structures

The most exciting feature of TFEL display is that it is all solid state, as shown in figure 2-2. The basic ACTFEL device structure has a metal-insulator-semiconductor-insulator-metal (MISIM) thin film configuration. These films are typically deposited on transparent glass substrates. Corning 7059 glass is especially used for devices processed below 650 °C because of its low cost and availability. Alternatively, NEG glass can be used for higher processing temperatures.

The first layer deposited on the glass substrate is commonly a transparent conducting oxide (TCO) which plays a role as a bottom electrode. The most common TCO material is indium tin oxide (ITO) with a resistivity of  $\sim 5 \text{ } \Omega/\square$  for a thickness range of 300 – 500 nm. Typically, ITO bottom electrode layers are deposited by sputtering. Subsequent to the TCO deposition, a transparent bottom insulator (250 – 500 nm), a

semiconducting phosphor (500 – 1000 nm), and a transparent top insulator (250 – 500 nm) are deposited, respectively. Finally a top metal layer is deposited (100 – 200 nm), which commonly serves as both an electrode and an optical reflector. Aluminum is frequently used as the top electrode material because of its high reflectivity as well as its processibility.

### 2.3 ACTFEL Device Physics

As illustrated schematically in Figure 2-3, the creation of luminescence in ACTFEL devices can be most easily described by breaking up the process into several parts. These are as follows [9].

- (1) INJECTION: Above the threshold voltage, electrons are injected from the interface states between the phosphor layer and insulating layer by high-field-assisted tunneling
- (2) TRANSPORT: The injected electrons are accelerated by the applied field and gain kinetic energy large enough to excite luminescent centers or the host lattice.
- (3) IMPACT EXCITATION: High-energy electrons, which are called hot electrons, directly excite luminescent centers through the impact-excitation mechanism.
- (4) RADIATIVE RECOMBINATION: When these electrons in the excited states of the luminescent centers make radiative transitions to the ground state, EL emission is realized. In other words, these luminescent centers relax radiatively and emit a photon. Alternatively, the centers may relax through a non-radiative pathway and emit a phonon.

- (5) ELECTRON TRAPPING: The hot electrons travel through the phosphor layer and are finally trapped at the phosphor layer/insulator layer interface states on the anode side, causing polarization.
- (6) When the polarity of the ac voltage wave forms is reversed, the same process takes place in the opposite direction in the phosphor layer.

## 2.4 ACTFEL Device Materials

### 2.4.1 Substrate

High transmission coefficient in the visible spectrum, thermal expansion coefficient that matches that of the deposited films, and high electrical resistivity are all desirable qualities for ACTFEL devices [1]. Also, low alkali metal content is required to avoid contamination by diffusion of these EL-killing impurities. Corning 7059 glass is typically used as a substrate due to cost and availability factors, although its low softening temperature ( $\sim 598^{\circ}\text{C}$ ) prohibits severe thermal processing. Corning 7059 glass is a non-alkaline, phosphosilicate glass with high thermal resistivity. If the EL phosphor requires a high temperature anneal, a glass-ceramic substrate may be required.

### 2.4.2 Transparent Conducting Electrode

As the name implies, high transmittance in the visible light region and large conductivity values are key qualities of these device layers. Indium tin oxide (ITO:  $\text{In}_2\text{O}_3$ -10wt% $\text{SnO}_2$ ) is typically used for this application. Since ITO can be easily etched by normal lithographic techniques, it is suitable for fine patterning ( $\sim 8$  lines/mm), necessary for high-information content flat panel displays. Care must be taken to achieve the optimum oxygen concentration for the ITO film since high conductivity of ITO is due

to oxygen deficiency. Oxidizing environment proceeds to reduce the degree of oxygen deficiency, resulting in high resistance. As the degree of oxygen deficiency increases, precipitation of metal fine particles and blackening of the film take place, leading to decrease in transmittance.

#### 2.4.3 Dielectrics

The performance of an ACTFEL device is strongly dependent on the quality and properties of the insulating layers themselves as well as the properties of the insulator/active layer interface [10]. The most important role of the insulators is to protect the phosphor layer from electric breakdown in the electric field of more than  $2 \times 10^6$  V/cm, so that insulator films must have no significant pinholes and defects in areas in excess of  $200 \text{ cm}^2$ . High dielectric constant, high dielectric breakdown strength, good adhesion, and self-healing breakdown capability are also desirable when selecting a dielectric material. In addition, the properties of the insulator/active layer interface are important since, from the interface states, electrons are injected into the conduction band of the phosphor layer through tunneling when the applied electric field is larger than the threshold electric field. Furthermore, the insulators must prevent metal-ion diffusion into the phosphor layer since alkali-metal ions deteriorate the EL performance.

#### 2.4.4 ACTFEL Phosphors

EL phosphor materials are composed of host and luminescent centers.

##### 2.4.4.1 Host Materials

Host materials must have a large enough bandgap to emit visible light from the luminescent center without significant absorption. They also must hold a high electric

field of the order of  $10^6$  V/cm without electric breakdown and have insulating characteristics below the threshold voltage. II-VI sulfides, such as ZnS, SrS, and CaS, are most commonly used as host materials for ACTFEL device applications since they exhibit high brightness and relatively low threshold voltages [10].

Table 2-1. Thin-film insulating materials typically used in ACTFEL devices. Included are dielectric constant, dielectric breakdown field, figure of merit (charge storage capacity), and breakdown mode.

Material	Deposition Method	$\epsilon$	$E_{BD}$ ( $10^8$ V/m)	Figure of Merit ( $\mu\text{C}/\text{cm}^2$ )	Breakdown Mode
SiO <sub>2</sub>	Sputtering	4	6	2	Self-healing
SiON	Sputtering	6	7	4	Self-healing
SiON	PCVD	6	7	4	Self-healing
Al <sub>2</sub> O <sub>3</sub>	Sputtering	8	5	3.5	Self-healing
Al <sub>2</sub> O <sub>3</sub>	ALE	8	8	6	Self-healing
Si <sub>3</sub> N <sub>4</sub>	Sputtering	8	6-8	4-6	Self-healing
SiAlON	Sputtering	8	8-9	5-6	Self-healing
Y <sub>2</sub> O <sub>3</sub>	E-beam	12	3-5	3-5	Self-healing
BaTiO <sub>3</sub>	Sputtering	14	3.3	4	Self-healing
BaTa <sub>2</sub> O <sub>6</sub>	Sputtering	22	3.5	7	Self-healing
Ta <sub>2</sub> O <sub>5</sub>	Sputtering	25	1.5-3	3-7	Self-healing
TiO <sub>2</sub>	ALE	60	0.2	1	Propagating
SrTiO <sub>3</sub>	Sputtering	140	1.5-2	19-25	Propagating
PbTiO <sub>3</sub>	Sputtering	150	0.5	7	Propagating

#### 2.4.4.2 Luminescent Centers

Luminescent centers must be properly incorporated into the host materials and emit visible lights. A large cross section is desirable for impact excitation. They also must be stable in the high electric field of the order of  $10^6$  V/cm. Transition metals and rare earth elements are typically used as a luminescent center. Transition metal ions, such as

$Mn^{2+}$ , show intrashell transitions of d-d transitions. RE ions including  $Tb^{3+}$ ,  $Tm^{3+}$ ,  $Ce^{3+}$ , etc. exhibit intrashell transitions of f-f or f-d transitions [11].

## 2.5 Rare-Earth Luminescent Centers

Rare earth (RE) elements have found wide use in a variety of light-emitting applications, from RE-doped fibers for infrared transmission to upconversion lasers to the phosphors found in CRTs and FPDs [12]. In particular, the ability of RE ions to emit red, green, and blue light make them well-suited for application in visible full-color display technologies. And also RE elements are known to sharply emit light at specific wavelengths independent of the host, which is due to atomic transitions between its 4f energy levels, as shown in Figure 2-4 [12].

The RE elements occupy a very special position among elements because of their unique outer electron configuration, which includes two unfilled orbitals, shown in Table 3-1. Lanthanum ( $Z = 57$ ) and lutetium ( $Z = 71$ ), the first and last of the lanthanide series, take the place of the first 5d transition element, both having the valence electron configuration  $5d^1 6s^2$  around the closed shells of the xenon core. For the elements following lanthanum, the 4f orbital is progressively filled with up to 14 electrons [13].

The 4f orbitals of the REs are screened from the environment by the outer 5s, 5p, and valence orbitals, as demonstrated by the radial density distribution of the outer electrons of the Gd atom [14], as shown in figure 2-5. The spatial seclusion of the partially filled 4f orbital within the xenon core and the screening of this orbital by two closed outer shells is a unique property of the lanthanides and motivates the interest in their unique physical and chemical properties.

In ACTFEL phosphors, the impact excitation dominates where excitation of the RE activator occurs by energy absorption from an elastic collision between a hot electron and the ground state 4f electrons in the RE activator. The electron is made hot before the elastic collision by acceleration by an electric field of magnitude 1-2 MV/cm. This results in a significant fraction of the electrons possessing energies greater than that necessary to excite the electron from the RE 4f ground state to higher 4f states or to the 5d states within the atom.

Table 2-2. The lanthanide series.

Element		Atomic #	RE <sup>3+</sup> ionic radius (Å)	Electronic configuration	RE <sup>3+</sup> ground state
La	Lanthanum	57	1.061	[Xe]4f <sup>0</sup> 5d <sup>1</sup> 6s <sup>2</sup>	<sup>1</sup> S <sub>0</sub>
Ce	Cerium	58	1.034	[Xe]4f <sup>1</sup> 5d <sup>1</sup> 6s <sup>2</sup>	<sup>2</sup> F <sub>5/2</sub>
Pr	Praseodymium	59	1.013	[Xe]4f <sup>3</sup> 6s <sup>2</sup>	<sup>3</sup> H <sub>4</sub>
Nd	Neodymium	60	0.995	[Xe]4f <sup>4</sup> 6s <sup>2</sup>	<sup>4</sup> I <sub>9/2</sub>
Pm	Promethium	61	0.979	[Xe]4f <sup>5</sup> 6s <sup>2</sup>	<sup>5</sup> I <sub>4</sub>
Sm	Samarium	62	0.964	[Xe]4f <sup>6</sup> 6s <sup>2</sup>	<sup>6</sup> H <sub>5/2</sub>
Eu	Europium	63	0.950	[Xe]4f <sup>7</sup> 6s <sup>2</sup>	<sup>7</sup> F <sub>0</sub>
Gd	Gadolinium	64	0.938	[Xe]4f <sup>7</sup> 5d <sup>1</sup> 6s <sup>2</sup>	<sup>8</sup> S <sub>7/2</sub>
Tb	Terbium	65	0.923	[Xe]4f <sup>9</sup> 6s <sup>2</sup>	<sup>7</sup> F <sub>6</sub>
Dy	Dysprosium	66	0.908	[Xe]4f <sup>10</sup> 6s <sup>2</sup>	<sup>6</sup> H <sub>15/2</sub>
Ho	Holmium	67	0.894	[Xe]4f <sup>11</sup> 6s <sup>2</sup>	<sup>5</sup> I <sub>8</sub>
Er	Erbium	68	0.881	[Xe]4f <sup>12</sup> 6s <sup>2</sup>	<sup>4</sup> I <sub>15/2</sub>
Tm	Thulium	69	0.869	[Xe]4f <sup>13</sup> 6s <sup>2</sup>	<sup>3</sup> H <sub>6</sub>
Yb	Ytterbium	70	0.858	[Xe]4f <sup>14</sup> 6s <sup>2</sup>	<sup>2</sup> F <sub>7/2</sub>
Lu	Lutetium	71	0.848	[Xe]4f <sup>14</sup> 5d <sup>1</sup> 6s <sup>2</sup>	<sup>1</sup> S <sub>0</sub>



## 2.6 Sulfide-based ACTFEL Phosphors

Since sulfide-based phosphors have dominated in performance, production, and research for ACTFEL device flat panel displays applications, a brief overview of these phosphors, with the main emphasis on the performance of blue-emitting ones, is provided in this section.

Zinc sulfide (ZnS) and alkaline-earth sulfides including calcium sulfide (CaS) and strontium sulfide (SrS) are the most common sulfide-based phosphors employed in ACTFEL flat panel displays [1]. They have been found to satisfy the basic requirements as TFEL phosphor host materials since they have a large enough band gap to emit visible light from the doped luminescent centers without significant absorption, and also, they can be a medium for the efficient transport of high energy ( $> 2$  eV) electrons. Therefore, these phosphors have exhibited excellent EL properties including high brightness and relatively low threshold voltages.

Monochrome ACTFEL displays based on ZnS:Mn were commercialized in the early 80s and their performance has been continuously improved up to now. This was possible because the yellowish-orange light-emitting ZnS:Mn thin film phosphor shows the highest brightness and luminous efficiency. Its luminescence level and luminous efficiency are reported to be up to  $300 \text{ cd/m}^2$  at 60 Hz and  $2 - 4 \text{ lm/W}$  at 1 kHz, respectively [1]. This can be explained by the fact that Mn ion has both the right valence (+2) and a similar ionic size to the Zn ion (only 8% difference) in the ZnS lattice. Ionic radii of  $\text{Zn}^{2+}$  and  $\text{Mn}^{2+}$  are 0.74 and 0.80 Å, respectively. As a result, Mn can be distributed uniformly in ZnS by substituting very nicely even at low process temperatures, and thus, large impact cross section ( $2 \times 10^{-16} \text{ cm}^2$ ) is realized [1].

In order to fabricate the full-color ACTFEL display devices, other sulfide-based TFEL phosphors for three primary colors (red, green, and blue) have been quite extensively studied so far. As for red emission, bright red light can be achieved by filtering the yellow emission from ZnS:Mn with a thin film red filter. Tuenge and Kane [4] reported a bright red emission by using an inorganic thin film long wavelength pass filter made of cadmium sulfoselenide (CdSSe).

ZnS:Tb,F has been found to be the brightest and most promising green-emitting ACTFEL phosphor. The ZnS:Tb,F was originally developed by Kahng [15] in 1968 and is called LUMOCEN (LUMinescent from MOlecular CENter) because the luminescent centers are expected to be in the form of TbF<sub>3</sub> molecules. Since then, the brightness and efficiency of ZnS:Tb,F have been improved by optimizing F/Tb ratio, adding another charge compensator such as oxygen, and introducing co-dopants such as Ag, Cu, Ce, etc.

The biggest and the most challenging problem is to find a satisfactory blue TFEL phosphor. Several sulfide-based phosphors, such as ZnS:Tm, SrS:Ce, SrS:Cu, and CaGa<sub>2</sub>S<sub>4</sub>:Ce, have been studied as a potential candidate for a blue-emitting ACTFEL phosphor. ZnS:Tm has a very good blue color purity with  $x=0.11$  and  $y=0.09$  since the line emission at 450 nm from the  $^1D_2 \rightarrow ^3F_4$  transition of trivalent thulium (Tm<sup>3+</sup>) matches well the saturated primary blue. Its luminance level was, however, very low with 2 cd/m<sup>2</sup> at 1 kHz driving [1]. SrS:Ce is an alkaline-earth blue-emitting TFEL phosphor. It is possible to obtain a pure blue EL emission by using a blue filter, but 80 to 90 % of the original luminance is lost. Typically, SrS requires a higher processing temperature and is more chemically unstable than ZnS [1]. The cerium-doped alkaline earth thiogallate-based phosphors including CaGa<sub>2</sub>S<sub>4</sub>:Ce, SrGa<sub>2</sub>S<sub>4</sub>:Ce, and BaGa<sub>2</sub>S<sub>4</sub>:Ce have been reported

as blue ACTFEL phosphors. Among them,  $\text{CaGa}_2\text{S}_4\text{:Ce}$  has demonstrated sufficient stability, luminance and blue chromaticity without the need for filtering enabling the fabrication of full-color TFEL panels [16]. However, a major disadvantage of these phosphors is that their complex crystal structure requires a high processing temperature ( $>650^\circ\text{C}$ ) to grow or convert to good crystalline material [16]. Recently, it has been found that  $\text{SrS:C u}$  is a reasonably efficient ( $0.2\text{ lm/W}$ ) blue phosphor with a good blue chromaticity ( $x=0.17, y=0.16$ ) [17]. This was a very surprising discovery to many people, because the traditional CRT phosphor,  $\text{ZnS:C u}$ , is not an efficient EL phosphor. Subsequent studies of the  $\text{SrS:C u}$  indicate that the  $\text{Cu}^{+1}$  ion forms a local center in  $\text{SrS}$  rather than a donor acceptor pair center as it does in  $\text{ZnS}$ . The different character of the  $\text{Cu}$  dopant center in  $\text{SrS:C u}$  enables this material to be an efficient EL phosphor [18]. However, as already mentioned, in the case of alkaline earth sulfide phosphor films, a thermal annealing at higher than  $800^\circ\text{C}$  is required to improve crystallinity of the film and to obtain high luminance.

### 2.7 III-Ntride-based TFEL Phosphors

While sulfide-based phosphors have dominated in performance, production, and research for ACTFEL device flat panel displays applications because they exhibit high brightness and relatively low threshold voltages, they have intrinsic problems such as chemical instability and sensitivity to moisture, which make it difficult to pattern the phosphors by chemical etching or photolithography. In addition, owing to their chemical instability, particularly in regard to moisture, sulfide ACTFEL devices degrade within a short time when operated in the atmosphere. As a result, at present, long-term operation

of ZnS phosphor TFEL devices has only been achieved by both the application of a double-insulating-layer structure and the use of a suitable device-sealing technique [1].

In the past few years, rare earth (RE)- or transition metal (TM)-activated III-V nitrides, such as GaN and AlN, have received an increasing amount of attention due to their unique properties such as higher chemical and thermal stability than sulfide-based phosphors. [6,7] In addition, III-V nitrides, such as GaN and AlN are reported to be an excellent phosphor host material for use in the full-color ACTFEL display devices since they have a large enough bandgap to emit visible light from the luminescent center without significant absorption. And moreover, they are found to incorporate RE atoms at concentration levels comparable to that possible with II-VI sulfide hosts including ZnS [8]. Also, III-V nitrides possess the ability to incorporate the trivalent RE ions without violating charge neutrality. Thus charge compensators used in ZnS:RE<sup>3+</sup> phosphors to avoid crystal defects, which may reduce both the excitation and radiative de-excitation efficiencies, are not needed in III-V nitrides:RE<sup>3+</sup> phosphors.

Phosphors based on III-V nitride host materials were first realized when visible emission was observed from Er-doped GaN, shown in Figure 3-1, by Steckl and Birkhahn [6]. The GaN was grown by molecular beam epitaxy on sapphire substrates using solid sources (for Ga, Al, and Er) and a plasma gas source for N<sub>2</sub>. Above GaN band-gap photoexcitation resulted in strong green emission. The emission spectrum consists of two narrow green lines at 537 and 558 nm and a broad peak at light blue wavelengths (480–510 nm). The narrow lines have been identified as Er transitions from the <sup>2</sup>H<sub>11/2</sub> and <sup>4</sup>S<sub>3/2</sub> levels to the <sup>4</sup>I<sub>15/2</sub> ground state.

Since this initial breakthrough, a number of rare earth (RE)- or transition metal (TM)-activated III-V nitride thin film phosphors have been studied. Visible, room-temperature photoluminescence (PL) and cathodoluminescence (CL) emission from various RE elements (Er, Tm, Eu, Dy, Pr, and Tb) have been observed in GaN [8]. In addition to PL and CL, Steckl and co-workers [19] have observed strong visible room-temperature electroluminescence (EL) emission from the Schottky light emitting diodes (LEDs) employing  $\text{Er}^{3+}$  (green),  $\text{Pr}^{3+}$  (red), and  $\text{Tm}^{3+}$  (blue) doped GaN, as shown in Figure 2-6.

Metal-organic chemical vapor deposition (MOCVD) and molecular beam epitaxy (MBE) have been used to grow the GaN host films. [19-21] The RE impurities were typically incorporated into the MOCVD- or MBE- grown GaN host by *in-situ* doping during the growth or by ion implantation after the growth. [19-21] However, those methods are relatively expensive and difficult to scale-up, which may hinder the fabrication of large-scale devices. A few researchers have sputter-deposited (SD) RE-doped GaN films. [22,23] However, only PL and CL emissions from SD GaN films doped with rare earths have been reported by these groups. In the present study, we demonstrated the first observation of visible and near-infrared electroluminescent light emission from sputter-deposited GaN doped with rare earth elements. The sputter deposition technique for growth of RE-doped GaN films offers a potential path for fabricating large-scale optoelectronic devices emitting in the visible and NIR ranges.

### 2.7.1 Gallium Nitride Host

Gallium nitride belongs to the family of III-V nitrides [24]. Some of the important physical properties of GaN are listed in Table 4-1. GaN has a number of attractive

properties such as a wide direct bandgap (3.4 eV at room temperature), good chemical and thermal robustness, excellent high field transport properties, and incorporates RE impurities at relatively high concentrations. GaN also possesses the ability to incorporate the trivalent RE ions without violating charge neutrality [19]. In addition, unlike in narrower bandgap semiconductors, in GaN no significant thermal quenching of the RE-related luminescence activity is observed up to temperatures as high as 550 K (275 °C). It is known to exist in hexagonal wurtzite ( $\alpha$ ) and cubic zinc-blende ( $\beta$ ) crystal polyphases; however most of the tabulated data exists only for the wurtzite form since the cubic structure is only meta-stable [25]. Wurtzite is a stable form in which the atoms are slightly displaced from their cubic-structure positions and form a crystal of hexagonal symmetry, as shown in Figure 2-7. Each atom has tetrahedral coordination of nearest neighbors.

### 2.7.2 Rare Earth Activators in Gallium Nitride

In order for GaN to be a visible- or near-infrared-emitting electroluminescent phosphor, various rare earth impurities have been incorporated into the GaN thin films deposited by radio frequency planar magnetron sputtering. Erbium (Er), thulium (Tm), europium (Eu), and neodymium (Nd) have been selected in the present study. Partial energy diagrams of these rare earth ions in trivalent state are shown in Figure 2-6.

Table 2-3. Physical properties of GaN\*

Atomic concentration	$8.9 \times 10^{22} \text{ cm}^{-3}$
Melting point ( $^{\circ}\text{C}$ )	> 2000
Lattice constant	a=3.189 Å c=5.185 Å
Dielectric constant	8.9 (Static) 5.35 (high frequency)
Refractive index	2.4
Density ( $\text{g/cm}^3$ )	6.15
Electron mobility	300 $\text{cm}^2/\text{V sec}$ (wurtzite) 1000 $\text{cm}^2/\text{V sec}$ (zinc-blende)
Bandgap (eV)	3.39 (direct)
Breakdown field (MV/cm)	>1.5
Thermal conductivity ( $\text{W cm}^{-1} \text{ K}^{-1}$ )	2

\*all data for wurtzite structure

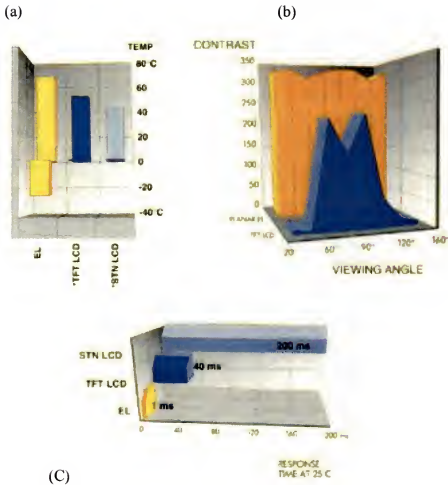


Figure 2-1. Performance of TFELDs in comparison with competing LCDs (a) temperature range, (b) viewing angle, (c) response time. [Planar Systems Inc.]



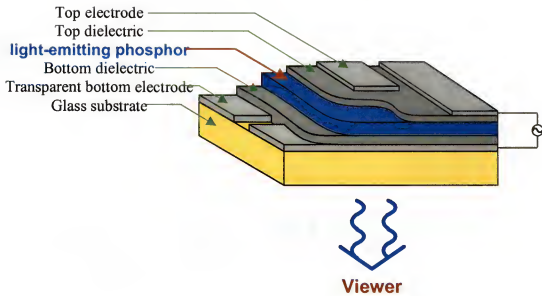


Figure 2-2. Conventional structure of a double-insulating-layer type ACTFEL device.

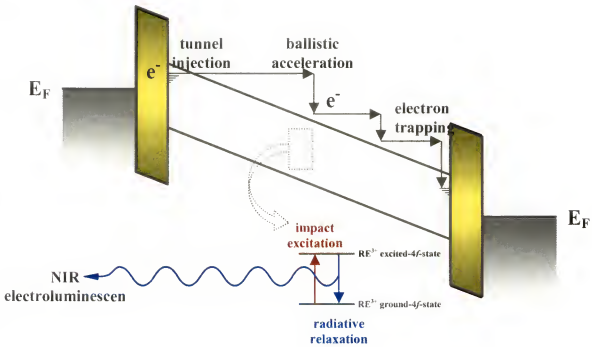


Figure 2-3. Energy band diagram of ACTFEL device with double insulating layers and the EL emission mechanism by impact-excitation of  $RE^{3+}$  ions.

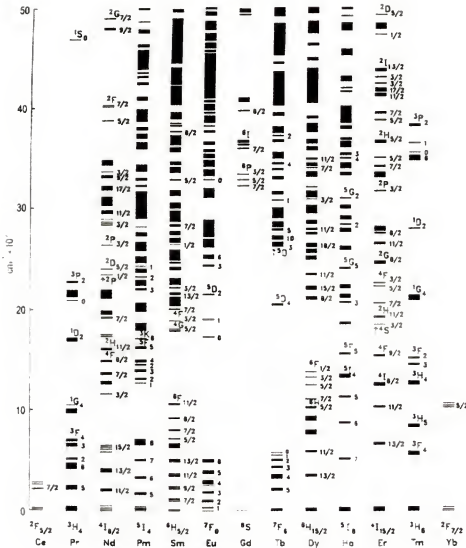


Figure 2.4 Energy band levels of the  $4f^n$  configurations of the trivalent lanthanide ions. The thickness of the line indicates the predicted crystal field splitting of the different energy levels [13].

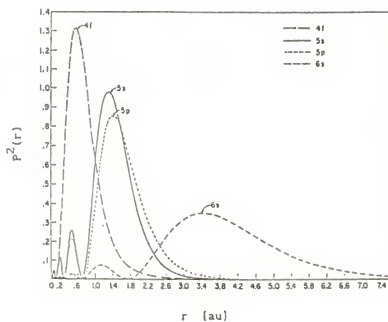


Figure 2-5. Square of the radial wave functions of Gd atom showing that the 4f electron orbital lies well inside the outer filled 5s and 5p orbitals (1 au = 0.529172 Å) [14].

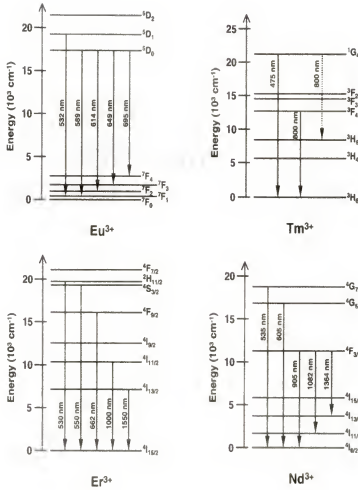


Figure 2-6. Partial energy diagrams of trivalent rare earth ions of Eu, Tm, Er, and Nd.

## CHAPTER 3 EXPERIMENTAL PROCEDURES

Preparation of rare earth-doped GaN ACTFEL devices includes GaN sputter target preparation, thin film sputter deposition, heat treatment, and ACTFEL device preparation. Characterization of the devices includes the optical, electrical, microstructural, and compositional characterization.

### 3.1 Gallium Nitride Thin Film Deposition

An extensive variety of film growth techniques, such as molecular beam epitaxy (MBE), metal-organic chemical vapor deposition (MOCVD), and hydride vapor phase epitaxy (HVPE), have been used to grow GaN films [25,26]. However, a relatively simple technique, sputter deposition (SD), which offers the possibility of large-area deposition with higher throughput, has not been used very successfully. In the present study, GaN thin films were grown by radio frequency planar magnetron sputter deposition.

Figure 3-1 shows a schematic diagram of the radio frequency (RF) planar magnetron sputtering system, which was used in the present study. Samples are inserted into the main growth chamber via loadlock chamber. Rare earth-doped GaN thin films were grown by co-sputtering of separate GaN and metallic Er targets in a pure nitrogen atmosphere. The targets were bonded to a water-cooled copper plate and covered with a movable shutter. The growth chamber was a cryo-pumped stainless-steel vessel and substrates were loaded through a load-lock chamber pumped by a turbomolecular pump.

Initially, the growth chamber was evacuated to a base pressure of less than  $2 \times 10^{-7}$  Torr and then throttled during the gas admission. Ultra-high-purity (99.999%)  $N_2$  gas flow was controlled by a MKS mass flow controller. No intentional substrate heating was employed and substrates were rested on a water-cooled stainless-steel platter during the film growth. This configuration minimized any heating by plasma radiation and/or by ion and secondary electron bombardment. Immediately before deposition, both targets were presputtered for 20 min with the shutter closed. The RF power inputs to the GaN and Er targets were 15 W and 20 W, respectively. Nitrogen gas pressure was kept constant at 15 mTorr throughout the film growth. The duty cycle applied to the RE target were varied in order to change the RE concentration in the deposited GaN host films. Table 3-1 shows the typical parameters used for co-sputter deposition of RE-doped GaN films. After the film growth, the samples were annealed at 700 °C in ultra-high-purity nitrogen ambient for 1 hour.

### 3.2 Rare-earth-doped GaN ACTFEL Device Fabrication

The substrates used for this research were Corning 7059 glasses, which were pre-coated with a 250 nm-thick indium-tin-oxide (ITO) bottom transparent electrode layer and a 200 nm-thick alumina-titania ( $Al_2O_3$ - $TiO_2$ , ATO) bottom dielectric layer. Figure 3-2 shows a schematic illustration of the half-stack RE-doped GaN ACTFEL devices. The ACTFEL devices were constructed with thin-film multilayered structure consisting of 250 nm-thick Al, 500 nm-thick RE-doped GaN, ATO, and ITO layers. The Al dot contact layer was thermally evaporated. The ATO dielectric layer, grown by atomic layer deposition (ALD), is used to prevent the catastrophic electrical breakdown during the

current flow. Thin films of ITO, a degenerated *n*-type semiconductor, were deposited by sputtering and used as a transparent conducting electrode.

Table 3-1. Sputter deposition parameters of GaN thin films doped with rare earths

GaN target material	GaN compound target
RE target material	Metallic RE target
Target diameter	2.5 cm
Processing gas	Ultra-high-purity N <sub>2</sub>
Working gas pressure	7 – 50 mTorr
Duty cycle for RE target	0 – 100 %
Duty cycle for GaN target	100 %
Base pressure	$1 \times 10^{-7}$ Torr
RF power for GaN	15 W
RF power for RE	20 W
Substrate	Si wafer, glass
Substrate temperature	Room temperature
Film thickness	400 - 500 nm

### 3.3 Rare-earth-doped GaN Heat Treatment

Heat treatment was required to optically activate the rare earth luminescent centers in GaN host films. The RE-doped GaN electroluminescent thin-film phosphors were grown at room temperature. Activation of the rare earth dopant-impurities can



normally be achieved upon annealing at high temperature. It is clear that the post-deposition thermal treatment have a significant effect on the electroluminescent characteristics of the TFEL display devices. This is because, as is well known, it not only recrystallizes the phosphor layer, but also activates the dopants. However, the non-stoichiometry problem and interdiffusion among the stacked structures would be two important issues for the thermally annealed devices, especially using the traditional furnace annealing process. Thus, decreasing the annealing time and increasing the process temperature are expected to benefit the post-deposition treatment results. Rapid thermal processing (RTP), which involves ramp-up rates on the order of 100 – 500 °C/s, is widely used in the thin film manufacturing process to activate dopants while at the same time minimize the dopant diffusion that occurs during the thermal processing. Therefore, in this study, the post-deposition thermal heat treatment will be carried out at various temperatures through rapid thermal processing. RE-doped GaN thin-film electroluminescent phosphors deposited on glass/ITO/ATO were annealed in ultra-high-purity nitrogen ambient at atmospheric pressure by a lamp-based furnace. The annealing temperature and time was 700 °C and 1 hour, respectively.

### 3.4 Characterizations

The information about the structural and compositional characterization is given in Section 3.4.1. The information about photoluminescence (PL) and electroluminescence (EL) is given in Section 3.4.2. Electrical characterization procedure is described in Section 3.4.3.

### 3.4.1 Structure and Composition Analyses

In so far as the luminescence of TFEL phosphors is strongly related to their properties including microstructure, crystallinity, composition, film density, etc., material characterization of the RE-doped GaN phosphor is essential in better understanding of the correlation between structure, properties, and luminescence of RE-doped GaN phosphor thin films. In this work, the sputter-deposited RE-doped GaN phosphor thin films will be characterized by a variety of methods.

#### 3.4.1.1 X-ray Diffraction (XRD)

X-ray diffraction (XRD) analysis has been performed on the samples to examine the crystalline structure of the RE-doped GaN phosphor layer. In addition to providing a quick measure of crystalline quality, XRD analysis also yields information on the crystalline lattice structure as well as phase identification and phosphor film texture. Phillips APD 3720 x-ray diffractometer will be used for quick evaluation. In addition, grazing incidence-angle XRD (GIXRD) will be carried out using X'Pert system since the diffraction peaks originating from the underlying layers and substrates can be avoided by using GIXRD analysis. Crystallinity of the RE-doped GaN phosphor layer can be also estimated by the full width at half maximum (FWHM) of x-ray diffraction peak. The grain size  $D_{hkl}$  can be evaluated from the Scherrer equation [27] as

$$\beta = \frac{K\lambda}{D_{hkl} \cos \theta},$$

where  $\theta$  is the diffraction angle,  $K$  the shape factor (taken as 1.05),  $\lambda$  the wavelength of the x-ray (1.54056 Å for Cu  $K_{\alpha}$ ), and  $\beta$  the FWHM of the particular XRD peak.

### 3.4.1.2 X-ray Reflectivity (XRR)

XRR measurement is a non-destructive method to obtain thickness, roughness, and density of thin films. X'Pert will be used for XRR measurement. Most materials have a refractive index  $n < 1$  for radiation with x-ray frequencies. This implies that at a grazing angle of incidence less than a value known as the critical angle  $\theta_c$ , x-rays are specularly reflected from most surfaces with very high efficiency representing the phenomena of total external reflection. The critical angle is proportional to the wavelength of the radiation  $\lambda$  and to the square root of the surface density,  $\rho$ : [28]

$$\theta_c = \lambda \sqrt{\rho},$$

where  $\theta_c$  is typically between  $0.25^\circ$  and  $0.75^\circ$ . As the angle is increased beyond  $\theta_c$  the reflectivity drops dramatically and is virtually 0 for  $\theta_c > 3\theta_c$ . The rate of decrease is determined by the microroughness of the sample, being proportional to  $\theta^{-4}$  for a perfectly smooth sample and decreasing even faster for a rougher sample.

### 3.4.1.3 Scanning Electron Microscopy (SEM)

The larger grain size typically results in better transport properties of electrons through the polycrystalline active layer. The care, however, must be taken in this case to minimize the roughness of the phosphor layer, associated with the larger grains. Therefore, comparative estimation of the crystallinity of the phosphor layer, SEM analysis may be performed. And also, cross-sectional morphology and thickness of the RE-doped GaN films can be examined using SEM.

#### 3.4.1.4 Atomic Force Microscopy (AFM)

It is desirable to have a very smooth interface between the various film layers because of the high field nature of TFEL devices. Any asperity will lead to a high field region that may lead to localized breakdown of the device structure. In contrast to SEM, the quantitative roughness value of the film surface can be obtained by using AFM. Typically root mean square (RMS) roughness value is used.

#### 3.4.1.5 Compositional Analyses

Energy dispersive spectroscopy (EDS) will allow the quick evaluation of composition in RE-doped GaN thin-film electroluminescent phosphor layers. More precise compositional evaluation can be accomplished by electron microprobe analysis (EPMA). However, it is more time-consuming. Auger electron spectroscopy (AES) and x-ray photoelectron spectroscopy (XPS) can be also used to measure Ga/N concentration ratio. In particular, the chemical bonding nature can be analyzed by XPS.

### 3.4.2 Photoluminescence and Electroluminescence Characterizations

#### 3.4.2.1 Photoluminescence

When the rare earth-doped GaN thin-film phosphor is struck by a light source at certain wavelength, an electron of a luminescent center in the phosphor material is excited to a higher energy state before it relaxes back to the ground state, emitting a photon. This process is called photoluminescence (PL) because the excitation source is light. PL can be used to characterize both the transitions leading to excitation as well as

emission. In the present study, a He-Cd laser at 325 nm was used to excite the RE-doped GaN thin-film phosphors.

#### 3.4.2.2 Electroluminescence (Brightness vs. Voltage Curve)

Brightness versus voltage (B-V), also called luminance versus voltage (L-V) curves, are the most important characterization methods for ACTFEL devices [3]. The typical B-V curve is schematically plotted in Figure 3-3. A B-V curve contains the following information about the ACTFEL device.

- (1) The threshold voltage, which is the  $B = 0$  intercept of the maximum slope tangent.
- (2) The  $B_{40}$  value, which is the brightness corresponding to the threshold voltage plus 40 V. It is commonly used to characterize the brightness of a device.

#### 3.4.2.3 CIE Coefficients

The color of light emitted by the phosphor is obviously another important issue to address when designing an ACTFEL display. The Commission Internationale de l'Eclairage (CIE) coordinates,  $x$ ,  $y$ , and  $z$ , are used to characterize color of emission [11]. Normally,  $x$  and  $y$  are obtained from the emission spectra, and the  $z$  value is defined by the other two in

$$x + y + z = 1. \quad (\text{Equation 3-1})$$

A standard CIE diagram is shown in Figure 3-4. The color gamut of ACTFEL displays that is achieved by the combination of the three primary colors, blue, red, and green from a particular set of phosphors, can be determined by plotting the coordinates ( $x$ ,  $y$ ) on the CIE diagram.

#### 3.4.2.4 Luminous Efficiency

The efficiency of light generation is another important property to characterize the ACTFEL device performance is the luminous efficiency ( $\eta$ ) [3]. The luminous efficiency ( $\eta$ ) is simply calculated by dividing the brightness (B) measured in either foot-Lambert (fL), nit ( $\text{cd}/\text{m}^2$ ), or watts by power density (W), as given in Equation 4-1.

$$\eta(\text{lm}/\text{W}) = \frac{B(\text{cd}/\text{m}^2)}{P(\text{W}/\text{m}^2)} \times \pi \quad (\text{Equation 3-2})$$

where B is the brightness and P is the power density, assuming an ideally diffuse emission surface. This is commonly accomplished by obtaining the  $B_{40}$  from the B-V curve and then measuring the power at 40 V above threshold from a charge-voltage plot. Luminous efficiency characterizes how much of the applied electric energy has been converted into light.

#### 3.4.3 Electrical Characterizations (Charge vs. Voltage Diagram)

A typical charge vs. voltage (Q-V) diagram is shown in Figure 3-5. For voltages below the threshold voltage, the Q-V diagram is a straight line, and the slope of the straight line is the capacitance of the series combination of the insulator and phosphor layers [10]. Above threshold, the diodes begin to conduct and the slope of the Q-V diagram now increases to the capacitance of the insulator layers alone, since the capacitance of the phosphor layer is now shorted out. The charge transported across the phosphor layer is stored at the phosphor/insulator interface and creates an internal polarization field that opposes the field generated by the externally applied voltage. The charge at the interface continues to build up until the voltage across the diode drops

below threshold at which time the charge transport is terminated. When the external charge is reduced, the voltage across the diodes remains below threshold, and thus, the charge transported remains at the interface, and the magnitude of this charge is represented by the value of  $Q$  for  $V = 0$ . This non zero value of  $Q$  for  $V = 0$  leads to a  $Q$ - $V$  curve that “opens up” into a parallelogram for voltages above threshold. The area inside this parallelogram represents the energy dissipated in generating the light from the ACTFEL device.

The following information can be obtained from this measurement [29]

- (1) The threshold voltage of the device and the threshold voltage of the phosphor layer.
- (2) The total capacitance of the three capacitors (two insulators,  $C_{in1}$  and  $C_{in2}$ , and a phosphor,  $C_{ph}$ ) before the voltage reaches the threshold voltage.
- (3) The total capacitance of the two insulator capacitors when the voltage is above the threshold voltage.
- (4) The amount of charge that transports across the phosphor  $\Delta Q$ , and that accumulates at the anode phosphor/insulator interface  $Q'$ .
- (5) The total power dissipated in the device after a cycle of operation. It is the area encompassed within the  $Q$ - $V$  diagram.

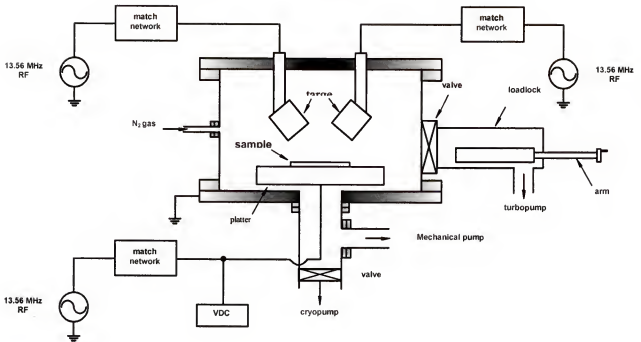


Figure 3-1. The schematic illustration of the radio frequency (RF) planar magnetron sputtering system, which was used in the present study.



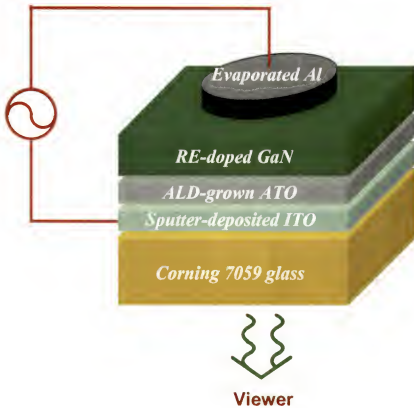


Figure 3-2. The structure of half-stack ACTFEL devices based on rare earth-doped GaN systems.

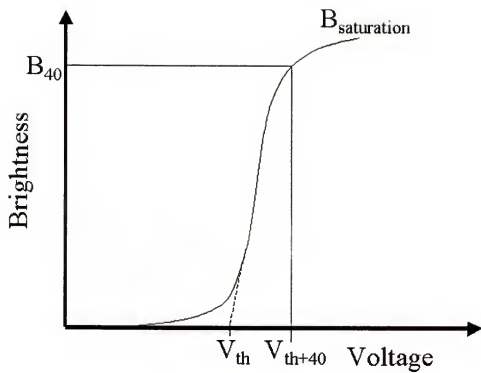


Figure 3-3. Schematic of brightness versus voltage curve [3].

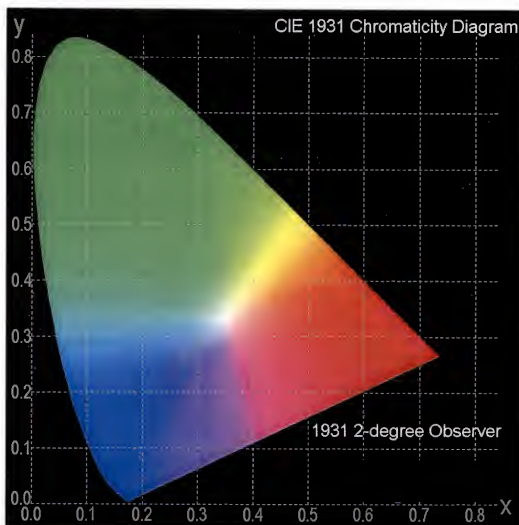


Figure 3-4. CIE 1931 chromaticity diagram.

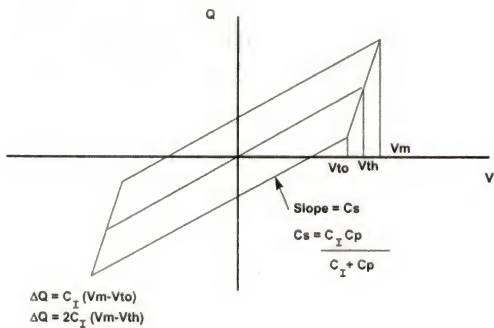


Figure 3-5. Q-V characteristics of an ACTFEL device [10].

## CHAPTER 4 STRUCTURE AND PROPERTIES OF GALLIUM NITRIDE THIN FILMS

### 4.1 Introduction

Gallium nitride (GaN) has been the focus of extensive research efforts due to its unique properties including wide direct bandgap, high thermal conductivity, high peak and saturation velocities, high electrical breakdown field, and thermal, mechanical, and chemical robustness [25]. GaN has a number of potential applications for the fabrication of a wide range of optoelectronic devices such as blue and ultra-violet (UV) light-emitting diodes (LEDs) and lasers, and UV photodetectors, as well as electronic devices for high power, high temperature, and high frequency operation [24]. In addition, room temperature ferromagnetism has recently been observed from GaN doped with Mn, suggesting applications of GaN material to spintronic devices [30]. Moreover, when doped with rare earth impurities, GaN emits light ranging from UV to visible to near-infrared, which makes it attractive for application in full-color flat-panel displays and fiber-optic telecommunications [19,20].

GaN crystallizes in either a thermodynamically stable wurtzite ( $2H$ ) structure having hexagonal symmetry with space group  $P6_3mc$  ( $C_{6v}^4$ ) or a metastable zinc-blende ( $3C$ ) structure with cubic symmetry with space group  $F43m$  ( $T_d^2$ ) [25]. Ga and N atoms in both wurtzite and zinc-blende structures are tetrahedrally coordinated with each other. In the crystallographic point of view, the wurtzite and zinc-blende GaN structures differ only in an altered stacking sequence of identical close-packed atomic planes [25]. For the

wurtzite structure, the stacking sequence of (0001) planes is ABABAB... in the [0001] direction while for the zinc-blende structure, the stacking sequence of (111) planes is ABCABC... in the [111] direction. The vast majority of research on GaN films has been focused on the hexagonal wurtzite form of GaN [26]. GaN in cubic zinc-blende form is also of great interest because it is predicted to possess superior electronic and material properties for device applications [31]. For instance, zinc-blende GaN is expected to have higher saturated electron drift velocity as a result of weaker phonon scattering due to its higher crystallographic symmetry than wurtzite counterpart [25]. Zinc-blende GaN is also expected to be easier to dope. In addition, zinc-blende GaN films can be cleaved along with the substrate facet, which is of great advantage to preparing cavity mirrors for laser diodes. Also, zinc-blende GaN allows the use of silicon as a substrate, which offers the possibility of realization of future GaN devices on the well-developed Si integrated circuit technology [31]. Moreover, a theoretical model recently proposed by Dietl *et al.* of the ferromagnetic behavior of Mn-doped *p*-type GaN predicts that the Curie temperature,  $T_c$ , for zinc-blende GaN is higher than that for wurtzite GaN [32].

Other group-III nitrides including aluminum nitride (AlN), indium nitride (InN), and boron nitride (BN) also exist in different crystalline structures such as hexagonal and cubic forms. While the mechanisms responsible for the phase transition of these group-III nitride thin films have been intensively studied, understanding of the phase transition and phase stability of GaN thin films remains quite primitive yet. In this section, we report on the observation of the room-temperature phase transformation in GaN thin films from the thermodynamically stable hexagonal wurtzite to the metastable cubic zinc-blende structure. The GaN films were grown on (100)- and (111)-oriented silicon substrates by

radio frequency (RF) planar magnetron sputter deposition. The role of hyperthermal species impinging on the film surface on the stabilization of the non-equilibrium zinc-blende GaN phase at room temperature is discussed. The experimental procedure for sputter deposition of GaN thin films has been given in Section 3.1.

## 4.2 Experimental Results

### 4.2.1 Phase Transition in GaN Thin Films

Figures 4-1 and 4-2 show the x-ray diffraction  $\theta$ - $2\theta$  scans obtained from the GaN films grown on Si (100) and (111) substrates, respectively, at nitrogen gas pressures ranging between 7 and 50 mTorr. The sharp diffraction peaks observed at around  $33.1^\circ$  in Figure 4-1 and  $28.4^\circ$  in Figure 4-2 originate from the Si substrates. In the GaN films grown at 50 mTorr, two distinctive diffraction peaks can be clearly observed at  $34.6^\circ$  and  $36.9^\circ$ . These are accounted for by the Bragg diffraction from the (0002) and  $(10\bar{1}1)$  planes of hexagonal wurtzite GaN phase, respectively [33]. This indicates that the GaN films grown at 50 mTorr have a polycrystalline hexagonal wurtzite structure. As the nitrogen gas pressure is decreased, two successive changes can be seen in the XRD patterns shown in Figures 4-1 and 4-2. First, the intensity of  $(10\bar{1}1)$  peak of wurtzite phase is gradually decreased and finally it is not detectable from the GaN films grown at pressures  $\leq 10$  mTorr. Second, the shoulder at the lower  $2\theta$  for the (0002) peak of wurtzite phase grows larger as the pressure is reduced and finally the low-angle shoulder becomes a dominant peak at pressures  $\leq 10$  mTorr. As shown in Figure 4-3, the peak at the lower  $2\theta$  angle side of the wurtzite (0002) peak can be ascribed to the Bragg diffraction from the (111) crystallographic plane of cubic zinc-blende phase of GaN. The

interplanar distance of zinc-blende (111) plane is slightly larger than that of wurtzite (0002) plane, resulting in a reduced Bragg angle [34]. The results obtained from XRD studies clearly reveal that as the nitrogen gas pressure during film growth is reduced from 50 to 7 mTorr, the crystalline phase in the GaN films transformed from a thermodynamically stable hexagonal wurtzite to a metastable cubic zinc-blende phase with (111) crystallographic planes oriented preferentially parallel to the film surface. It should be also noted that the orientation of the Si substrates is not a factor in determining the phase of the grown GaN films. Also, since the GaN films were grown at room temperature, the thermally-driven processes are not of any major importance in determining the phase. Thus, it can be speculated that the evolution of the non-equilibrium cubic zinc-blende GaN phase must result mainly from the intrinsic growth-related effects.

Figure 4-4 presents the variation in the relative XRD intensity ratio of zinc-blende (111) to wurtzite (0002) peak,  $I_{\text{ZB}(111)}/I_{\text{W}(0002)}$ , as a function of the nitrogen gas pressure. The  $I_{\text{ZB}(111)}/I_{\text{W}(0002)}$  intensity ratio is slowly increased as the pressure is reduced from 50 mTorr. At pressures below  $\sim 15$  mTorr, the  $I_{\text{ZB}(111)}/I_{\text{W}(0002)}$  ratio sharply increases. These data suggest that the wurtzite to zinc-blende phase transformation is associated with a threshold phenomenon. It can be noticed that upon decreasing the gas pressure below the threshold pressure of  $\sim 15$  mTorr, cubic zinc-blende phase becomes dominant in GaN films.



#### 4.2.2 Internal Stress of GaN Thin Films

In Figures 4-1 and 4-2, it can be noticed that the positions of Bragg diffraction peaks originating from the GaN films are gradually shifted to the lower  $2\theta$  values as the pressure is decreased while the positions of the (100)- and (111)-oriented Si substrate peaks at  $33.1^\circ$  and  $28.4^\circ$  remain constant. This reveals that the degree of lattice strain is increased upon decreasing the nitrogen gas pressure. The expansion of the spacing between the planes parallel to the film surface corresponds to a contraction in the plane of the surface, indicating a biaxial state of compressive stress, rotationally symmetric with respect to the surface normal. From the results of XRD measurements, it can be speculated that the GaN films grown at lower pressure are under larger biaxial compressive stress conditions.

The internal film stresses can be calculated from the measurement of the net strain induced in the Si substrates by the GaN films using the well-known Stoney's formula. Figure 4-5 shows the dependence of the internal film stresses on the nitrogen gas pressure. The internal stress plotted in Figure 4-5 represents the sum of the intrinsic stress and the thermal stress in the films. The intrinsic stress is the part of the film stress which is built in during the film growth. The thermal stress is a result of the mismatch of the thermal expansion coefficients of the film and the substrate as the sample cools from the deposition temperature to room temperature. Since the Si substrates were in contact with a water-cooled stainless-steel platter during the film growth, the thermal strain resulting from differential thermal contraction of the GaN film and the Si substrate is not likely to occur in our case. Thus, the observed changes in the internal stress result mainly from changes in the intrinsic growth-related strain. As can be seen in Figure 4-5, the GaN films

grown at 50 mTorr are under a slightly tensile stress ( $\sim 0.43$  GPa) in the plane of the surface. As the gas pressure is reduced, the tensile stress gradually diminishes to zero and the stress is converted from tension to compression at 25 mTorr. The observed transition of the stress from tensile to compressive upon decreasing the gas pressure can be attributed to a phenomenological atomic peening [35] mechanism. At pressures below 15 mTorr, the compressive stress rapidly increases and reaches a value of  $\sim 3.1$  GPa at 7 mTorr.

#### 4.2.3 Microstructure Evolution of GaN Thin Films

The microstructure of the grown GaN films was studied in fractured cross section and plan view using a field emission scanning electron microscopy (FESEM). Figure 4-6 shows the cross-sectional FESEM images of the GaN films grown at different gas pressures. As shown in Figure 4-6(a), the GaN films grown at 50 mTorr exhibit a columnar microstructure in which the voided boundaries surround the columns. The columns are approximately 70 nm in average width. At 15 mTorr, as can be seen in Figure 4-6(b), the GaN films are composed of tightly packed columnar grains with less voided boundaries. Finally at 7 mTorr, as shown in Figure 4-6(c), the voided regions have completely disappeared and the films exhibit an extremely dense, fibrous microstructure with little discernible structural features on both surface and cross section. The observed changes in microstructure of the GaN films from a voided to tightly packed columnar, and then to a extremely dense fibrous structure is a synergistic result of the changes in the energy, flux, and incidence angle of the particles impinging on the growing film upon varying the gas pressure. This will be discussed in detail below.

#### 4.3 Discussion

Sputter deposition is a conceptually and experimentally simple, yet highly versatile tool for the fabrication of thin-film materials, especially those which exhibit a metastable structure [36]. It is the hyperthermal species involved in the sputter deposition process that may create non-equilibrium growth conditions favorable for the formation of metastable phases. In the typical plasma-based sputter deposition processes such as diode, triode, and magnetron sputtering, the condensing film may be exposed to a significant flux of hyperthermal species, even in the absence of direct ion beam bombardment. These species include the fairly energetic sputtered target atoms, known to have energies averaging in the range of tens of electron volts, and predominantly neutralized gas atoms that are backscattered from the cathode target surface with larger energies potentially up to hundreds of eV. [37] It has been shown that the impact of these energetic species impinging on the surface of the growing films plays a crucial role on the stabilization of non-equilibrium phases such as cubic-BN, cubic-AlN, tetrahedral amorphous carbon ( $\alpha$ -C), and carbon nitride ( $\beta$ -C<sub>3</sub>N<sub>4</sub>) [38-40].

The impact energy of the hyperthermal species impinging on the growing films can be qualitatively controlled by judiciously manipulating the gas pressure during the sputter deposition. Since the energy of these species is much higher than the thermal energy of the ambient gas atoms, they gradually lose their excess energy as they repeatedly collide with gas atoms. At sufficiently high pressures, the initially high energy of the hyperthermal species is completely dissipated and they reach the thermal equilibrium with the ambient gas atoms. This phenomenon is referred to as thermalization. Thus, the kinetic energy of the impinging particles is a strong function of

the number of collisional gas-phase scattering which is inversely proportional to the mean free path,  $MFP$ . The  $MFP$  is larger at lower gas pressure,  $P_{nitrogen}$ , as described by the equation,  $MFP \approx 6.6/P_{nitrogen}$ , where  $MFP$  and  $P_{nitrogen}$  are in mm and Pa, respectively [41]. Accordingly, as the gas pressure during sputter deposition is reduced, the energetic species impinge on the surface of the growing film with higher energies since they undergo fewer inelastic gas-phase collisions in traveling over the distance between the target and the substrate. In addition, the self-bias voltage,  $V_b$ , of cathode target is increased with decreasing the gas pressure,  $P_{nitrogen}$ , as defined by the equation,  $V_b = k(W_{target}/P_{nitrogen})^{1/2}$ , where  $W_{target}$  is the RF power applied to the target and  $k$  is a coefficient depending on factors such as the electrode areas [36]. With the RF power fixed, the target self-bias voltage is higher at lower pressure, which can also be another factor in increasing the energy of the species that are back-reflected from the cathode target surface. Consequently, the bombardment-related processes induced by transferring the energy and momentum of the high-energy species to atoms condensing on the film surface become more pronounced at lower gas pressures. Also at lower pressure, the incoming particle flux is more directional due to the reduced collisional gas scattering in transit from target to substrate. Thus, the flux of particles arriving at normal incidence is larger at lower pressure, thereby reducing the atomic self-shadowing effect.

Combining the experimental results presented in Sections. 4-2-2 and 4-2-3, it can be found that the microstructural evolution of the GaN films was accompanied by a film stress transition from tensile to compressive upon decreasing the nitrogen gas pressure during the film growth. The GaN films grown at high pressures have a voided columnar microstructure and are in tension. The limited mobility of condensing atoms and atomic

self-shadowing are considered responsible for the development of a columnar, voided microstructure. This is true because the incoming particles reach the substrate at more oblique incidence angles and with lower energies at high pressures, as discussed above. The observed tensile stress is thought to be due to the interatomic attractive forces acting across the voids pulling the film columns together. In contrast, the GaN films grown at low pressures exhibit an extremely dense, fibrous microstructure and are in compression. As discussed above, upon decreasing the pressure, both the normal component in the incidence angle and the kinetic energy of the incoming particle flux increase. As a result, the atomic self-shadowing effect becomes less pronounced and the mobility of surface adatoms is enhanced, thereby suppressing the development of columnar growth. Also, at low pressures, the energetically bombarding particles transfer their momentum and energy to condensing atoms incorporated in the GaN film lattice, which causes a series of atomic displacement through the knock-on process, leading to microstructural densification by annihilation of porosity. Thus, the effect, called the atomic peening [35] action, becomes more pronounced at lower pressure, giving rise to an increase in the compressive stress in the films.

It is interesting to note by comparing Figures 4-4 and 4-5 that the abrupt increase in compressive stress from 15 to 7 mTorr coincides well with the rapid evolution of the non-equilibrium cubic zinc-blende phase of GaN. This striking correlation between phase and stress level leads to questions about the relationship between the two. Figure 4-7 shows the variation in the XRD peak intensity ratio of  $I_{\text{ZB}(111)}/I_{\text{W}(0002)}$  as a function of the average compressive stress in the films. The zinc-blende phase starts to form as the GaN films become compressively stressed, and there is a rapid increase in the zinc-blende

phase content at a threshold compressive stress of  $\sim 1$  GPa. The switching over from wurtzite to zinc-blende phase at a threshold compressive stress clearly indicates that the formation of the non-equilibrium cubic zinc-blende phase is triggered by the development of compressive stress in GaN films. The rise in internal compressive stress leads to an increase in the effective pressure in the GaN films. Thus, it is speculated that the internal compressive stress above the threshold value of  $\sim 1$  GPa drives the GaN material into a high-pressure regime in the phase diagram where the zinc-blende GaN phase is stable. It can therefore be concluded that the internal compressive stress induced by microstructural densification resulting from the impact of the hyperthermal species promotes the formation of the non-equilibrium cubic zinc-blende GaN phase at room temperature.

#### 4.3 Summary

Thin films of GaN were grown on (100)- and (111)-oriented Si substrates at room temperature by RF planar magnetron sputter deposition. X-ray diffraction measurements reveal that as the nitrogen gas pressure during film growth was decreased from 50 to 7 mTorr, the crystalline phase of the grown GaN films transformed from a thermodynamically stable hexagonal wurtzite to a metastable cubic zinc-blende phase. Along with the phase transformation, the strong dependence of the microstructure and internal stress of the GaN films on the nitrogen gas pressure was also observed. The microstructure of GaN films was altered from a voided to tightly packed columnar, and then to a extremely dense fibrous structure upon decreasing the gas pressure. While the GaN films grown at pressures  $\geq 30$  mTorr were under biaxial tensile stress, films grown

at lower pressures were in higher compression. It is speculated that the impact by the hyperthermal species impinging on the surface of growing GaN film has led to the microstructural densification, resulting in larger compressive internal film stress developed at lower pressures. It is found that the compressive stress above a threshold value of  $\sim 1$  GPa was sufficiently large to stabilize the non-equilibrium cubic zinc-blende phase of GaN at room temperature.

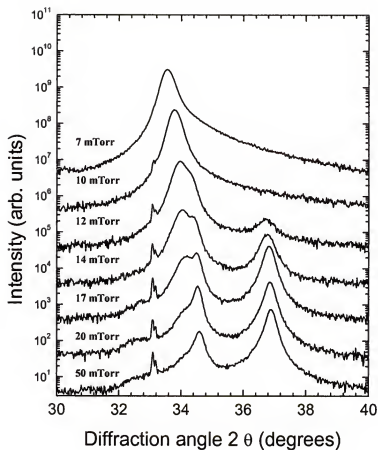


Figure 4-1. X-ray diffraction patterns of the GaN films grown on Si (100)-oriented substrates at various nitrogen gas pressures. The diffraction intensities are expressed on a logarithm scale. Patterns are vertically offset for clarity.



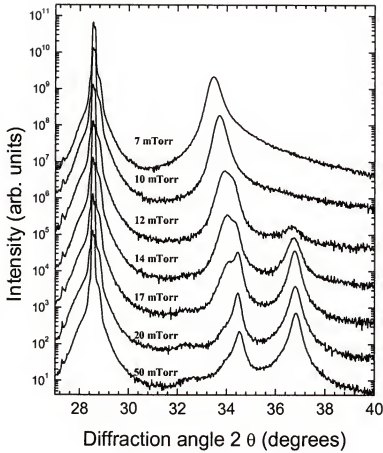


Figure 4-2. X-ray diffraction patterns of the GaN films grown on Si (111)-oriented substrates at various nitrogen gas pressures. The diffraction intensities are expressed on a logarithm scale. Patterns are vertically offset for clarity.

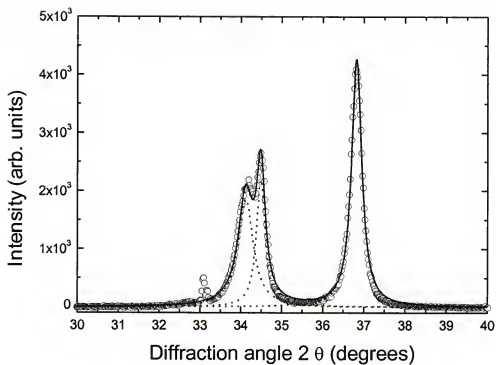


Figure 4-3. Peak deconvolution was performed to show the details of separation between the hexagonal wurtzite (0002) and cubic zinc-blende (111) Bragg diffraction peaks. The dotted and solid lines represent the experimentally acquired and fitted patterns, respectively.

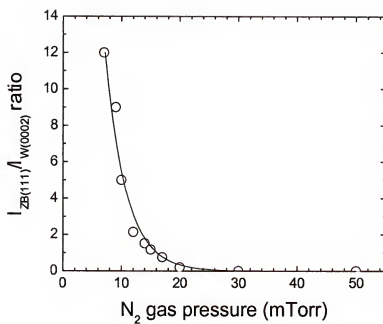


Figure 4-4. Variation in the XRD intensity ratio of the zinc-blende (111) to wurtzite (0002) peak as a function of the nitrogen gas pressure during film growth.

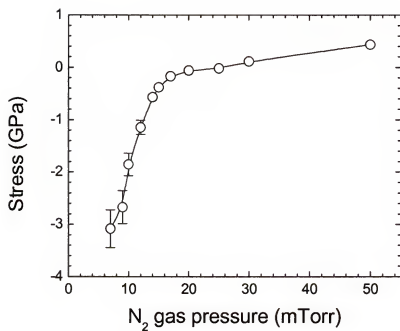


Figure 4-5. Dependence of the internal stress in the GaN films on the nitrogen gas pressure. Positive and negative values denote tensile and compressive stress, respectively.

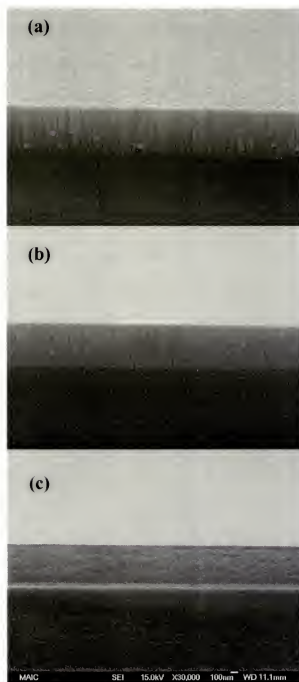


Figure 4-6. Cross-sectional field-emission scanning electron micrographs of the GaN films grown on Si (111) substrates at (a) 50, (b) 15, and (c) 7 mTorr.

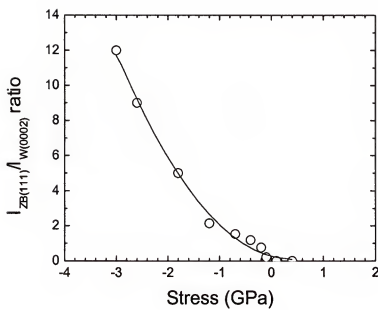


Figure 4-7. The variation in the XRD peak intensity ratio of  $I_{ZB(111)}/I_{W(0002)}$  as a function of the average compressive stress in the films

## CHAPTER 5 TEXTURED GROWTH OF CUBIC GALLIUM NITRIDE THIN FILMS

### 5.1 Introduction

Gallium nitride (GaN) has received a considerable amount of attention because its unique properties make it suitable for applications in optoelectronic devices such as blue and ultra-violet (UV) light-emitting diodes (LEDs) and laser diodes (LDs), UV photodetectors, as well as electronic devices operating at high temperatures and high power levels [26]. It is well known that GaN has two crystalline structures: a thermodynamically-stable wurtzite structure having hexagonal symmetry and a metastable zinc-blende structure with cubic symmetry [25]. The majority of work to date has paid attention to the hexagonal wurtzite form of GaN [24]. Recently, there has been a rapidly growing interest in the cubic GaN because of its attractive properties for device applications including higher saturated electron velocity and easier doping than the hexagonal counterpart [34].

It has been demonstrated that cubic GaN thin films can be grown on substrates with cubic symmetry, e.g., (001) Si, (001) GaAs, (001) MgO, and (001) 3C-SiC by using molecular beam epitaxy (MBE) and metal-organic chemical vapor deposition (MOCVD) [25]. However, sputter deposition (SD) has not been used to date for the growth of cubic GaN, although it is a conceptually and experimentally simple yet highly versatile tool for thin-film research. In this section, we report on the growth of cubic GaN films on silicon (100)-oriented substrates at room temperature by radio frequency (RF) planar magnetron sputter deposition. The growth of GaN on Si is of interest due to the potential for

incorporating GaN devices onto Si-based integrated circuits. The influence of film growth rate on the texture and properties of the cubic GaN films has been investigated. The experimental procedure for sputter deposition of GaN thin films has been given in Section 3.1.

## 5.2 Experimental Results and Discussion

### 5.2.1 Growth Rate of Cubic GaN Thin Films

Figure 5-1 shows the dependence of the growth rate of GaN films on the RF cathode target power. The film growth rate is increased almost linearly from 16 to 155 Å/min as the RF power is raised from 10 to 30 W. The observed linear relationship between the two can be explained by the rise of the cathode target potential,  $V_c$ , with increasing the RF cathode target power,  $W_{target}$ , as described by the equation,  $V_c = k(W_{target}/P_{nitrogen})^{1/2}$ , where  $P_{nitrogen}$  is the nitrogen gas pressure during the film growth and  $k$  is a coefficient depending on factors such as the electrode areas [36]. Since the nitrogen gas pressure,  $P_{nitrogen}$ , was fixed in the present work, the cathode target potential,  $V_c$ , is considered to be higher at higher RF target power,  $W_{target}$ , leading to higher energy of incident ions onto the GaN target. As a consequence, the sputtering yield is increased as the RF power is raised, thus producing thicker films.

### 5.2.2 X-ray Diffraction and Pole Figures

Figure 5-2 shows x-ray diffraction  $\theta$ - $2\theta$  scans of the GaN films grown at RF cathode target powers ranging between 10 and 30 W. In all the cases, a single Bragg diffraction peak is observed at  $\sim 33.7^\circ$ , which is attributed to the (111) plane of cubic zinc-blende GaN phase. The interplanar  $d_{(111)}$  spacing derived from XRD (2.65 Å) is



slightly larger than the reported value ( $2.62 \text{ \AA}$ ) for the (111) plane spacing of cubic GaN films grown by molecular beam epitaxy [34]. This larger interplanar distance can be ascribed to compressive stress in the films. As shown in Figure 5-3, the compressive stress in the GaN films, measured by Stoney's formula was found to be  $\sim 2 \text{ GPa}$  and did not change significantly with changes of the RF cathode target power. As demonstrated earlier in Chapter 4, the cubic GaN phase is stabilized at room temperature by the compressive stress which was built up in the GaN films during the growth. Note in Figure 5-2 however that the cubic (111) XRD peaks are slightly asymmetric at higher Bragg angles. We suggest that the asymmetry of the cubic (111) peak is due to a small fraction of wurtzite GaN embedded in the cubic structure. The position of the (0002) hexagonal peak is expected to be at  $2\theta$  of  $\sim 34.3^\circ$ . Thus, the separation of the hexagonal (0002) and the cubic (111) peaks is relatively small ( $\sim 0.6^\circ$ ), which could result in an asymmetry in the cubic (111) peak. The (111) peak position was used to determine the  $a$  lattice parameter of the cubic crystalline unit cell, approximately  $4.59 \text{ \AA}$ , again slightly larger than the reported values ( $4.54 \text{ \AA} \pm 0.02 \text{ \AA}$ ) for cubic GaN films grown by molecular beam epitaxy [42]. This is again attributed to the in-plane compressive stress present in the films.

The XRD data reveal that the cubic GaN films have a highly textured structure with (111) crystallographic planes oriented preferentially parallel to the substrate surface. This fact can also be confirmed by x-ray pole figure data. Figure 5-4 shows a (111) x-ray pole figure for the cubic GaN films grown at a RF cathode target power of 10 W. The intensity of the (111) reflection was collected for various setting of  $\phi$ ,  $\phi$  and  $\psi$ , at  $2\theta = 33.7^\circ$ . The center of the plot indicates the substrate normal. It is clear that the [111]

direction lies predominantly along the direction of the substrate normal and the peak is azimuthally symmetric. This unique central maximum of the (111) pole figure again indicates that the cubic GaN films have a strongly textured structure with the [111] direction perpendicular to the substrate surface. The [111] preferred orientation for cubic GaN films can be explained in terms of the surface energy. It has been commonly observed in vapor-deposited thin films that even if the initial nucleation creates grains which are randomly oriented, the films will rapidly transform during growth to a specific crystallographic orientation where the free surface has an atomic plane parallel to the surface that minimizes surface energy. Typically, this is a plane of high atomic packing density. In cubic zinc-blende structure of GaN, the (111) plane is close packed, having the lowest surface energy of the principal surfaces [42]. Thus, it is reasonable that the surface of cubic GaN films prefers to be the (111) plane.

### 5.2.2 X-ray Rocking Curves of Cubic GaN Thin Films

Figure 5-5 shows the x-ray rocking curves of the (111) reflections parallel to the cubic GaN film surface. The  $2\theta$  axis of the four-circle diffractometer was set at the angle characteristics of the (111) diffraction peak, which was  $33.7^\circ$ , and the omega,  $\omega$ , axis was scanned to obtain the rocking curves shown in Figure 5. The angular width of the rocking curve provides a measure of the perfection of the [111]-oriented crystallites in cubic GaN films. If the film consists of a collection of well [111]-oriented, high crystalline quality grains, the rocking curve will be narrow. As the misorientation of the grains relative to one another increases, the rocking curve will broaden. The full width at half maximum (FWHM) of the (111) rocking curve of cubic GaN films grown at RF cathode target

powers of 10, 20, and 30 W is measured to be  $4.51^\circ$ ,  $7.68^\circ$ , and  $8.73^\circ$ , respectively. These data clearly indicate that the degree of [111] preferred orientation and the crystalline quality is higher in the films grown at lower growth rates. During deposition, sputtered atoms condensing onto a substrate attempt to minimize the surface energy in the limited time that the atoms are mobile on the surface, prior to being frozen into a fixed position. It is therefore reasonable speculation that lower growth rates allow adatoms to migrate over longer distances, leading to crystalline grains that are more strongly [111]-oriented. In contrast, at higher growth rate, the adatoms may be buried by the succeeding deposition material before they reach the low surface energy lattice sites. Therefore, the cubic GaN films grown with higher rate are less strongly textured along the [111] direction.

### 5.2.3 Auger Electron Spectroscopy Analysis

Figures 5-6(a) – 5-6(c) present the Auger electron spectra obtained from cubic GaN films grown at RF cathode target powers of 10, 20, and 30 W, respectively. The spectra were collected after surface cleaning by 3 keV  $\text{Ar}^+$  ion beam for 1 min to remove any atmospheric contaminants. As can be seen, only oxygen was detected in the films and no other impurities were observed. Note that the oxygen peak intensity is higher in the GaN films grown at lower growth rates. In order to determine the source(s) of the oxygen impurity, Auger depth profile data were collected, as shown in Figures 5-7(a) – 5-7(c), from the films grown at RF cathode target powers of 10, 20, and 30 W, respectively. The profiles of Ga and N are stable throughout the film, indicating that the cubic GaN films were very uniform. The oxygen signal sharply decreased when the film surface was

sputtered away. This is due to removal of a thin gallium oxide and/or surface hydroxide layer which was formed on the GaN film surface due to exposure to the atmosphere. The small hump in the oxygen signal at the film-substrate interface originates from the surface oxide on the Si wafers. While it is not clear that the oxygen signal is above the noise level for films grown at 30 W, a real, uniform signal is clear for films grown at 10 and 20 W. A uniform oxygen concentration and its inverse correlation with the film growth rate strongly suggest that the oxygen was incorporated into the GaN films during sputter deposition rather than diffusing into the films after the growth or adsorbing during the AES analysis. The most likely source of impurities is residual oxygen in the vacuum system. The inverse correlation between oxygen content and film growth rate is believed to be due to the increased time for oxygen to be incorporated into the GaN films at lower growth rates. The apparent low nitrogen content of the films is due to the relative elemental sensitivity factors [43]. Another factor could be preferential sputtering, i.e., more rapid sputtering of nitrogen than of gallium, which typically causes problems in depth profiling and quantitative analysis for binary nitride compounds [44]. Note also in Figure 7 that although all the GaN films were approximately 5000 Å thick, the films containing a higher oxygen impurity content required a longer sputter time to reach the Si substrate interface. This is presumably due to lower sputter etch rate of Ga-oxygen versus Ga-nitrogen bonds.

### 5.3 Summary

Cubic GaN thin films were grown on silicon (100) wafers at room temperature by RF planar magnetron sputtering of a GaN target in a pure nitrogen ambient. The influence of film growth rate on the structure and properties of the cubic GaN films has

been investigated by changing the RF cathode target powers between 10 and 30 W. X-ray  $\theta$ - $2\theta$  diffraction and pole figure analyses showed that the grown GaN films had a predominant cubic phase with a strongly preferred crystallographic orientation of the [111] direction perpendicular to the film surface. X-ray rocking curve measurements revealed that cubic GaN films grown at lower growth rates exhibited better crystallinity and a more strongly [111]-textured structure. Oxygen impurities were incorporated during film growth at concentrations which were lower as the GaN growth rate was increased.

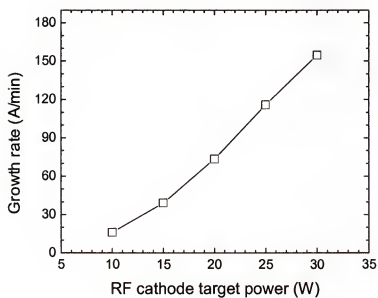


Figure 5-1. Dependence of the growth rate of cubic GaN films on the RF power applied to the GaN cathode target.

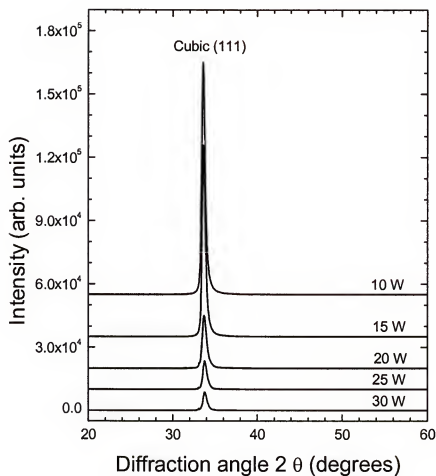


Figure 5-2. X-ray diffraction  $\theta$ - $2\theta$  scans for the cubic GaN films grown at different RF cathode target powers. Patterns are vertically offset for clarity.

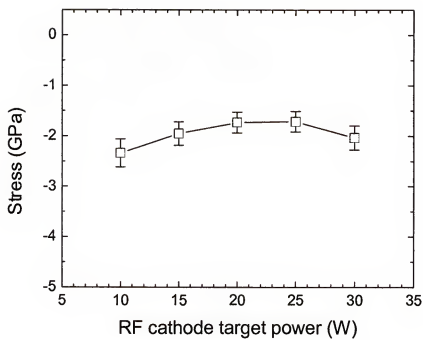


Figure 5-3. Internal stress in the GaN films as a function of the RF power applied to the GaN cathode target. Negative value denotes compressive stress.



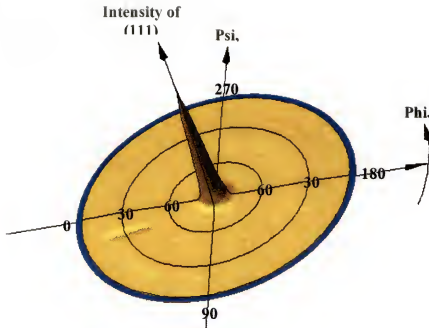


Figure 5-4. X-ray pole figure obtained from the GaN films grown at a RF cathode target power of 10 W. The center of the circle corresponds to the surface normal. The  $2\theta$  detector was set at the angle of (111) diffraction plane, which was  $33.7^\circ$ .

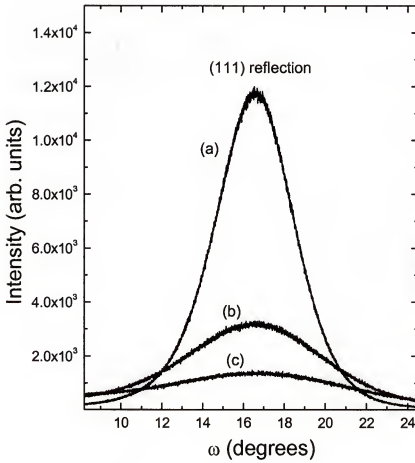


Figure 5-5. X-ray rocking curves for the (111) diffraction peak collected from the GaN films grown at RF cathode target powers of (a) 10, (b) 20, and (c) 30 W.

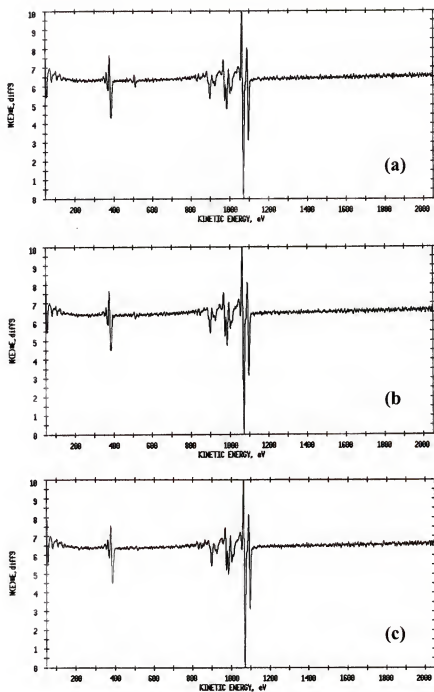


Figure 5-6. Auger electron spectra collected from the GaN films grown at RF cathode target powers of (a) 10, (b) 20, and (c) 30 W. Background pressure, electron beam energy, and current were  $< 1 \times 10^{-8}$  Torr, 5 keV, and  $5 \times 10^{-8}$  A, respectively. The surfaces were cleaned by  $\text{Ar}^+$  ion beam sputtering at 3 keV for 1 min.

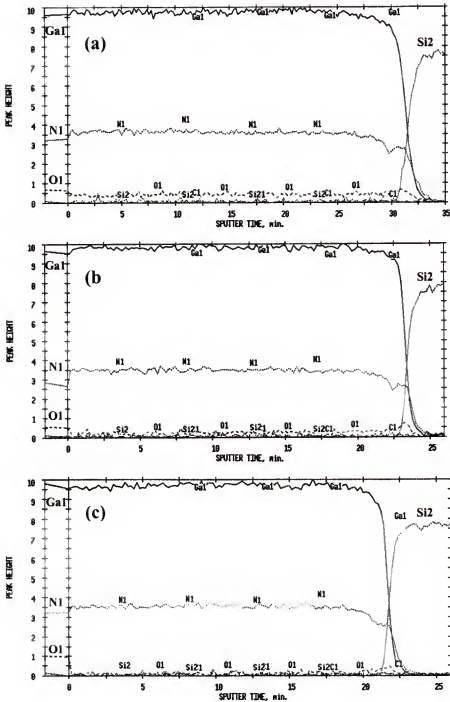


Figure 5-7. Auger depth profiles collected from the GaN films grown at RF cathode target powers of (a) 10, (b) 20, and (c) 30 W. Data were recorded for Ga, N, O, C, and Si in the intermittent sputtering mode.

## CHAPTER 6

### PHOTOLUMINESCENCE AND ELECTROLUMINESCENCE OF EUROPIUM-DOPED GALLIUM NITRIDE

#### 6.1 Introduction

Gallium nitride (GaN) continues to be of great interest due to its remarkable properties which make it suitable for applications in optoelectronic devices, such as light-emitting diodes (LEDs) for use in displays and solid-state lighting [26]. In LEDs, the dominant emission wavelength is determined by the bandgap of the active layer material, since the light emission results from radiative recombination of electron-hole pairs in band-edge or near-band-edge quantum states. The electrons and holes are injected by a forward voltage bias, and recombine in a quantum well or near a p-n junction [24]. This is sometimes called low field electroluminescence. Recently, rare earth (RE)-activated GaN higher field electroluminescent devices (ELDs) have attracted considerable research interest because of their potential applications in full-color flat-panel displays (FPDs). In these GaN ELDs, hot electrons generated by electric field typically  $> 1 \text{ MV/cm}$  result in impact-excitation of RE ground-state electrons to excited-state energy levels. De-excitation occurs by a radiative energy relaxation process, and photons may be emitted over a spectral range from ultraviolet (UV) to visible to infrared (IR) [19]. The emission wavelengths can be varied by changing the RE impurity-dopants, and red, green, and blue colors can be realized in a single GaN host ELD system [19].

In this section, we report on room temperature photoluminescence (PL) and electroluminescence (EL) from europium (Eu)-doped GaN thin films grown by radio

frequency (RF) planar magnetron co-sputter deposition. Sputter deposition (SD) is a conceptually and experimentally simple film-growth technique that may be scaled-up for large-scale flat-panel displays with high throughput and cost efficiency. Eu was chosen as the luminescent center in the present study since the radiative transition from the  $^5D_0$  excited-state to the  $^7F_2$  level in  $\text{Eu}^{3+}$  ions is known to produce a deep red color which is suitable for display applications [11]. The experimental procedure for sputter deposition of GaN thin films has been given in Section 3.1.

## 6.2 Experimental Results and Discussion

### 6.2.1 X-ray Photoelectron Spectroscopy Analysis

Based on x-ray diffraction data, the crystalline structure of Eu-doped GaN films was *c*-axis-oriented hexagonal wurtzite. Eu is a well-known mixed-valence element which has two valence states ( $\text{Eu}^{2+}$  or  $\text{Eu}^{3+}$ ). The valence state can be determined using the XPS binding energy position of the Eu  $4d$  core level, and the difference is known to be about 7 eV [45]. The  $4d$  peak from  $\text{Eu}^{3+}$  appears at a higher binding energy than does that from  $\text{Eu}^{2+}$  since  $\text{Eu}^{3+}$  has one less  $4f$  electron than  $\text{Eu}^{2+}$ , leading to a greater Coulombic attraction between the core hole and photoejected  $4d$  electron. The Eu  $4d$  core peak from GaN containing ~1.8 at.% Eu is shown in Figure 6-1, and consists of three resolved peaks at 128.9, 136.7 and 142.3 eV. The binding energies of the XPS peaks were referenced against the Ga  $2p_{3/2}$  peak fixed at 1117 eV for GaN. [54] The peaks at 136.7 And 142.3 eV are from the  $\text{Eu}^{3+} 4d_{5/2}$  and the  $4d_{3/2}$ , according to the XPS Handbook [45] and Vercaemst, *et al.* [46], who measured XPS data from  $\text{EuF}_3$ . The peak at 128.9 eV is probably from some  $\text{Eu}^{2+}$  on the sputter cleaned surface, and may be real or result from preferential sputter removal of N, leading to a reduction of the cationic

species [44]. It is unlikely that a significant fraction of the Eu is in the +2 valence state since this would result in a broad blue-green PL and EL emission from the  $\text{Eu}^{2+} 4f^6 5d^1 \rightarrow 4f^7 (^8S_{7/2})$  transition, [47] which was not observed (see Section 6.2.2).

### 6.2.2 Photoluminescence Properties of Eu-doped GaN

The PL spectrum obtained at room temperature from GaN doped with ~1.8 at.% of Eu is shown in Figure 6-2. Four emission peaks can be observed at 589, 614, 649, and 695 nm. They are attributed to the  $\text{Eu}^{3+} 4f-4f$  intrashell transitions of  $^5D_0 \rightarrow ^7F_1$ ,  $^5D_0 \rightarrow ^7F_2$ ,  $^5D_0 \rightarrow ^7F_3$ , and  $^5D_0 \rightarrow ^7F_4$ , respectively, as depicted in Figure 6-3 which shows the optical transition level diagram of the  $\text{Eu}^{3+}$  ion [13]. As mentioned above, no emission from  $\text{Eu}^{2+}$  ion was detected (strongest peak expected at around 500 nm) [47]. The wide PL band between 500 – 570 nm could originate from the commonly observed yellow emission due to impurities and defects, [48] which overlaps partially with the  $\text{Eu}^{3+}$ -related emission from the  $^5D_1 \rightarrow ^7F_1$  transition. The spectrum in Figure 6-2 shows that the intensity of the 614 nm peak, assigned to the  $^5D_0 \rightarrow ^7F_2$  transition, is much stronger than the 589 nm peak, attributed to the  $^5D_0 \rightarrow ^7F_1$  transition. The  $^5D_0 \rightarrow ^7F_2$  and  $^5D_0 \rightarrow ^7F_1$  are hypersensitive electric-dipole (ED) and magnetic-dipole (MD) transitions, respectively [49]. When the Eu ion is placed at a center of symmetry, ED transitions between the  $4f^6$  levels are strictly forbidden by the Laporte selection rule (equal parity) while MD transitions are allowed. [48]. Thus, the intensity of the  $^5D_0 \rightarrow ^7F_2$  transition is strongly dependent upon changes in local symmetry environment around the  $\text{Eu}^{3+}$  ion, while the  $^5D_0 \rightarrow ^7F_1$  intensity is relatively unaffected by this local environment. Accordingly, the intensity ratio of  $^5D_0 \rightarrow ^7F_2$  to  $^5D_0 \rightarrow ^7F_1$ , known as the asymmetry

ratio, would be zero when the Eu ion is at a center of perfect symmetry, but could be quite large for distorted sites. This ratio is a measure of the degree of distortion of the inversion symmetry of the  $\text{Eu}^{3+}$  ion site in the host lattice [49]. The asymmetry ratio of the ~1.8 at.% Eu-doped GaN films is ~3.3, indicating a significant amount of distortion of the inversion symmetry of the  $\text{Eu}^{3+}$  lattice sites. It has been reported that the  $\text{Eu}^{3+}$  ion is incorporated into the wurtzite GaN host by substitution on the Ga sub-lattice, which should have trigonal  $C_{3v}$  symmetry [19]. Therefore, there is a lack of inversion symmetry which produces strong ligand crystal fields and thereby relaxing the Laporte selection rule. Thus the probability of the  $\text{Eu}^{3+}$   $4f-4f$ /hypersensitive ED transitions increases, giving rise to the observed high asymmetry ratio.

Figure 6-4 shows the intensity of the 614 nm PL peak as a function of the concentration of the Eu in the GaN host films. The intensity sharply increases, is maximum at ~1.8 at.% Eu, and then decreases at higher concentrations presumably due to concentration quenching. At high Eu concentrations, cross relaxation between adjacent  $\text{Eu}^{3+}$  ions and/or energy transfer from  $\text{Eu}^{3+}$  ions to non-radiative recombination centers such as impurities, defects, and grain boundaries have been reported [11]. In addition, Eu doping deteriorates the crystallinity of the GaN host due to the large ionic radius of  $\text{Eu}^{3+}$  (0.97 Å) versus that of  $\text{Ga}^{3+}$  (0.62 Å) [50].

### 6.2.3 Electroluminescence Characteristics of Eu-doped GaN

The EL spectrum obtained at room temperature from the ~1.8 at.% Eu-doped GaN films is shown in Figure 6-5. The spectrum consists of a series of well resolved emission peaks in the region of 530 – 700 nm, analogous to the PL spectrum shown in



Figure 6-2. As mentioned above and also depicted in Figure 6-3, the EL peaks at 532, 588, 614, 648, and 696 nm are attributed to the  $\text{Eu}^{3+} 4f-4f$  intrashell transitions of  $^5D_1 \rightarrow ^7F_1$ ,  $^5D_0 \rightarrow ^7F_1$ ,  $^5D_0 \rightarrow ^7F_2$ ,  $^5D_0 \rightarrow ^7F_3$ , and  $^5D_0 \rightarrow ^7F_4$ , respectively [13]. The asymmetry ratio, defined above, is  $\sim 3.1$ , which is in reasonable agreement with the value obtained from the PL measurement. Similar room temperature EL spectra were reported by Steckl *et al.* [19] from Eu-doped GaN grown by molecular beam epitaxy (MBE). While sputter- and MBE-grown GaN:Eu films show similar luminescent spectra, there is a significant difference in the width and relative intensities of the peaks, presumably resulting from differences in crystallinity due to the growth technique. Since our sputter-grown GaN:Eu films are polycrystalline, emission peaks are broad and the Stark splitting is not resolved, in contrast to the MBE-grown, single-crystalline GaN:Eu.

The dependence of the EL peak intensities,  $I$ , versus applied AC peak voltage,  $V$ , measured from the  $\sim 1.8$  at.% Eu-doped GaN films is shown in Figure 6-6. The  $I$ - $V$  curves measured for four peaks (588, 614, 648, and 696 nm) had the same threshold voltage,  $V_{th}$ , of  $\sim 145$  V, but the 532 nm emission had a higher threshold voltage of  $\sim 155$  V. The threshold voltage is defined as the voltage axis intercept of the tangent to the  $I$ - $V$  data. The four peaks with the same threshold voltage all originate from the  $^5D_0$  excited level at  $17,270 \text{ cm}^{-1}$ , while the 532 nm peak originates from the higher-lying  $^5D_1$  state at  $19,030 \text{ cm}^{-1}$  (see Figure 6-3). It is reasonable to expect a larger threshold voltage for the 532 nm peak due to the requirement of a higher energy to impact-excite the  $\text{Eu}^{3+}$  ions into the  $^5D_1$  level. Higher threshold voltages for higher excited-states have been reported for other thin-film EL phosphor systems that are dominated by direct impact-excitation processes. [51]

### 5.3 Summary

Photoluminescence (PL) and electroluminescence (EL) were demonstrated at room temperature from Eu-doped GaN thin films grown by radio frequency (RF) planar magnetron co-sputter deposition. The highest intensity PL emission peak lies in the red region at ~614 nm, and results from the  $^5D_0 \rightarrow ^7F_2$  hypersensitive electric-dipole transition in the trivalent Eu ions. The optimum concentration of Eu for PL was determined to be ~1.8 at.%. The EL spectra, analogous to the PL spectra, consist of a series of well resolved emission peaks in the region of 530 – 700 nm, which originate from the  $^5D_J \rightarrow ^7F_{J'}$  ( $J = 0, 1$ ;  $J' = 1, 2, 3, 4$ ) transitions. Higher EL voltage was needed to excite  $\text{Eu}^{3+}$  ions into the higher-lying  $^5D_1$  state versus the lower-lying  $^5D_0$  state, consistent with EL excitation being dominated by direct impact by hot electrons.

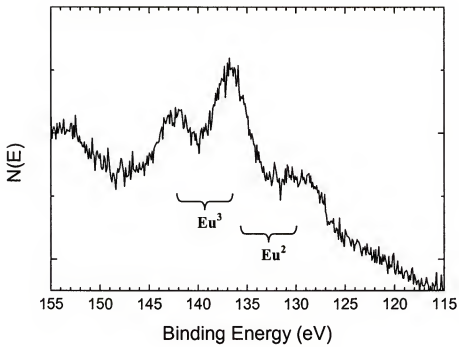


Figure 6-1. XPS spectrum of the Eu  $4d$  core level collected for  $\sim 1.8$  at.% Eu-doped GaN films.

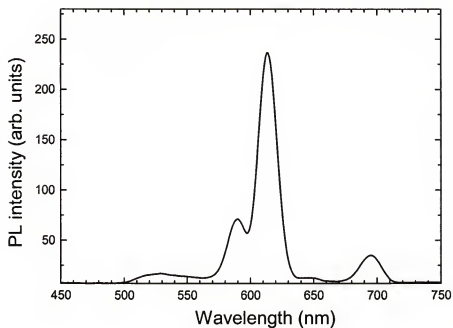


Figure 6-2. Photoluminescence (PL) spectrum recorded at room temperature from ~1.8 at.% Eu-doped GaN films.

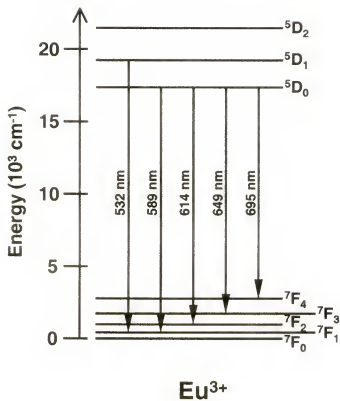


Figure 6-3. Partial energy level diagram for an  $\text{Eu}^{3+}$  ion [13]. Arrows represent the radiative transitions corresponding to the PL and EL peaks observed in the present work from the Eu-doped GaN films.

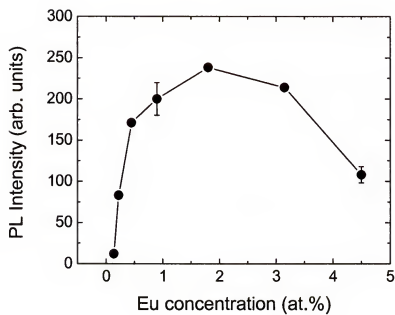


Figure 6-4. Dependence of the intensity of 614 nm photoluminescence emission peak on the concentration of Eu in GaN host films.

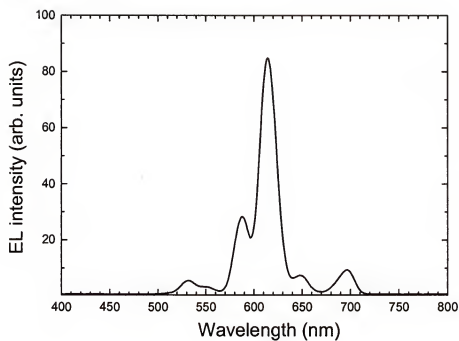


Figure 6-5. Electroluminescence (EL) spectrum emitted from ~1.8 at.% Eu-doped GaN films. The EL spectra were recorded at room temperature.

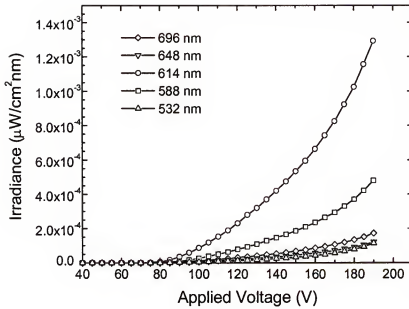


Figure 6-6. EL intensity versus applied AC peak voltage ( $I$ - $V$ ) data measured for peaks at 532, 588, 614, 648, and 696 nm from  $\sim 1.8$  at.% Eu-doped GaN films.



## CHAPTER 7 ELECTROLUMINESCENCE OF THULIUM-DOPED GALLIUM NITRIDE

### 7.1 Introduction

Rare-earth-activated gallium nitride (GaN:RE) has recently sparked considerable interest. RE elements generally have a partially-filled  $4f$  inner shell that is screened from its surroundings by completely-filled  $5s^2$  and  $5p^6$  outer shells. This gives rise to optical emission peaks which are relatively insensitive to the host lattice and are determined by the energy of the transition between  $4f$  states of the rare-earths. GaN is a wide bandgap semiconductor possessing a direct bandgap of 3.4 eV at room temperature, good thermal and chemical robustness, excellent high field transport properties, and incorporates RE impurities at relatively high concentrations [20]. Therefore, the combination of GaN with the unique properties of RE species could allow the development of a novel visible and near-infrared light emitter for practical applications in full-color flat-panel displays and optical fiber telecommunication systems [19,20].

Visible and near-infrared (NIR) photoluminescence (PL), cathodoluminescence (CL), and electroluminescence (EL) have been reported from GaN thin films doped with various RE impurities including Er, Eu, Pr, Tm, and Tb [19,48]. Metal-organic chemical vapor deposition (MOCVD) and molecular beam epitaxy (MBE) have been used to grow the GaN host films [19,48]. The RE impurities were typically incorporated into the MOCVD- or MBE- grown GaN host by *in-situ* doping during the growth or by ion implantation after the growth [19,48]. A few researchers have sputter-deposited (SD) RE-doped GaN films [22,23]. However, only PL and CL emissions from SD GaN films

doped with rare earths have been reported by these groups. In the previous chapter, we reported the first demonstration of EL from SD GaN:Eu. The sputter deposition technique for growth of RE-doped GaN films offers a potential path for fabricating large-scale optoelectronic devices emitting in the visible and NIR ranges. Here emission of blue and NIR photons during EL from SD GaN thin films doped with thulium (Tm) is reported. The dominant EL excitation mechanism of the Tm-doped GaN electroluminescent layer is also discussed below. The experimental procedure for sputter deposition of GaN thin films has been given in Section 3.1.

## 7.2 Experimental Results and Discussion

### 7.2.1 Electroluminescence Emission Spectra of Tm-doped GaN

Figure 7-1 shows an electroluminescence spectrum from a typical Tm-doped GaN ACTFEL device, exhibiting a near-infrared (NIR) emission peak at ~800 nm and a blue emission peak centered at ~475 nm. The blue emission peak can be assigned to a  $\text{Tm}^{3+}$  4*f*-intrashell transition from the  $^1G_4$  excited-state level to the  $^3H_6$  ground-state [13], as depicted in figure 7-2. The NIR peak can be associated with either the  $^1G_4 \rightarrow ^3H_5$  transition or the  $^3F_4 \rightarrow ^3H_6$  transition [52]. Another characteristic emission of  $\text{Tm}^{3+}$  luminescent centers originating from the  $^1G_4 \rightarrow ^3H_4$  transition (~650 nm) was not observed from our devices. Kato *et al.* [53] suggested that the probability of 650 nm emission due to the  $^1G_4 \rightarrow ^3H_4$  transition could be reduced by ion-pair relaxation between  $\text{Tm}^{3+}$  ions in ZnS host at a relatively high Tm concentration (> 1 at.%). The fact that this emission is not observed in the EL devices is consistent with this hypothesis since the present devices contain a rather high concentration of Tm (~1.5 at.%). The absence of the

650 nm transition suggests that the origin of the 800 nm emission peak is the  $^3F_4$  state rather than the  $^1G_4$  state, which is consistent with data discussed below.

### 7.2.2 Emission Intensity versus Voltage Curves

Figure 7-3 shows the dependence of the EL intensities,  $I$ , of the 475 and 800 nm emission peaks as a function of the AC peak voltages,  $V$ , applied to the devices. The  $I$ - $V$  data shown in Figure 7-3 were collected sequentially from the same device. The first  $I$ - $V$  curve was the 475 nm peak from the device versus an increase of the voltage, and then the voltage was reduced back to zero. Subsequently, the 2nd data set based on the 800 nm peak was collected, followed by the 3rd curve as a repeat of the 475 nm peak, and this was followed by the 4th, 5th, and finally 6th  $I$ - $V$  curves, respectively. All data were collected from the same device in the same way as the 1st curve was collected, except for the wavelength detected. All of the  $I$ - $V$  curves show that the intensities of both the blue and NIR emission peaks are increased as the AC voltage is raised above a threshold voltage. The threshold voltage,  $V_{th}$ , is typically defined as the voltage intercept of the extrapolation of the maximum slope of the  $I$ - $V$  curve back to zero intensity. The typical aging behavior for freshly fabricated ACTFEL devices can be seen by comparing subsequent  $I$ - $V$  measurements. Both blue and NIR peaks exhibit an increase in threshold voltage and a decrease in intensity at the same voltage for successive measurements of the same emission wavelength, i.e. with longer time of operation. As the device is aged longer,  $V_{th}$  and the intensity at the same voltage stabilizes. Both trends are typical of aging behavior for ACTFEL devices. The blue 475 nm emission shows a threshold voltage,  $V_{th}$ , of 161 - 167 V, while the NIR 800 nm emission has a  $V_{th}$  of 148 - 150 V. It should be noted that no matter how long the device is aged, the threshold voltage for the

NIR 800 nm peak is consistently 11 to 19 volts lower than that for the blue 475 nm peak. Since the distribution of hot electrons would shift to higher energies upon increasing the applied voltage, the lower threshold voltage for the NIR emission indicates that lower electron energies are needed to impact-excite the Tm ion into the NIR-emitting state. This result implies that the excited-state level responsible for NIR 800 nm emission is at a lower energy level than the  $^1G_4$  excited-state responsible for the blue 475 nm emission. Therefore, we attribute the NIR peak at 800 nm to the  $^3F_4 \rightarrow ^3H_6$  transition, since the  $^3F_4$  excited-state is a lower-lying  $4f$  level than the  $^1G_4$  state.

### 7.2.3 Electroluminescence Excitation Mechanisms

In the Tm-doped GaN electroluminescent layer, the  $\text{Tm}^{3+}$  ions may be excited either indirectly or directly. In the case of indirect excitation, electron-hole pairs in the GaN host lattice are generated by hot electron impact ionization, and the recombination energy of the electron-hole pairs is transferred to the  $\text{Tm}^{3+}$  luminescent centers, giving rise to light emission. If impact ionization was the dominant excitation mechanism in GaN:Tm ACTFEL devices, the EL intensity ratio of 475 nm to 800 nm,  $I_{475}/I_{800}$ , would not significantly depend on the applied voltage. This is true because the intensity ratio would depend mainly on the energy transfer efficiencies between the GaN conduction and valence bands and the excited levels of  $^3F_4$  and  $^1G_4$  on the Tm, convoluted with the electronic transition probabilities of  $^3F_4 \rightarrow ^3H_6$  and  $^1G_4 \rightarrow ^3H_6$  on the  $\text{Tm}^{3+}$  ions [51]. Neither of these processes would be expected to be strongly dependent upon the applied voltage and field. However, as can be seen in Figure 7-4, the EL intensity ratio,  $I_{475}/I_{800}$ , is increased by ~900% upon a 67% increase in the applied AC voltage (from 120 to 200

V). As discussed above and shown in Figure 7-2, the excited-state energy level corresponding to the 800 nm NIR transition ( $^3F_4$ ) is located below the  $^1G_4$  excited-state level responsible for the blue 475 nm emission. Since the EL intensity ratio,  $I_{475}/I_{800}$ , was found to depend significantly on the applied voltage, it is reasonable to assume that the dominant excitation process for EL from SD GaN:Tm ACTFEL devices is direct impact excitation of the  $\text{Tm}^{3+}$  luminescent centers. Direct impact excitation occurs by direct interaction between hot electrons and the  $^3H_6$  ground-state  $4f$  electrons, raising them to the excited states. This interpretation is consistent with the observations of other ACTFEL phosphor systems that are dominated by impact excitation processes [51].

The EL emission intensity,  $I$ , due to the impact excitation mechanism has often been described by the relation,  $I = I_0 e^{-bV^{-1/2}}$ , where  $I_0$  and  $b$  are constants, and  $V$  is the applied voltage [54]. The logarithm of the EL intensity,  $\ln(I)$ , versus the reciprocal square root of the applied AC voltage,  $V^{-1/2}$ , is plotted in Figure 7-5 for both of the 475 and 800 nm emission peaks. These plots show that EL intensity as a function of the applied voltage varies as  $V^{-1/2}$  for both peaks. This is additional evidence that direct impact excitation of the  $\text{Tm}^{3+}$  luminescent centers by hot electrons is the dominant excitation process. In general, the energy transfer probability by ionized electrons and holes under a high electric field ( $> 1 \text{ MVcm}^{-1}$ ) is very small since the electrons and holes rapidly separate under the action of the field unless they are trapped in a localized center [55]. The relative inefficiency of blue 475 nm versus 800 nm emission, as is evident from data in Figures 7-1 and 7-3, probably results from the difference in energy between the ground and excited states. The lower-lying  $^3F_4$  state requires less energy for excitation as compared to the higher-lying  $^1G_4$  state, and a larger fraction of the hot electrons would be

capable of exciting electrons to the lower lying state. The fraction of electrons sufficiently energetic to excite the  $^1G_4$  state would be reduced by inelastic scattering by electrons in the low-lying energy levels ( $^3H$  and  $^3F$ ) of the Tm ions.

### 7.3 Summary

Both visible and near-infrared light is emitted by alternating-current electroluminescence (EL) from sputter-deposited GaN thin films doped with Tm. The blue and NIR emission peaks at  $\sim 475$  and  $\sim 800$  nm, respectively, were attributed to  $\text{Tm}^{3+}$   $4f-4f$  intrashell transitions from the  $^1G_4$  or  $^3F_4$  excited-states to the  $^3H_6$  ground-state, respectively. The threshold voltage for 475 nm blue emission was consistently higher than that for 800 nm NIR emission. In addition, the EL intensity ratio of 475 nm to 800 nm emission peaks was dramatically increased with an increase in the applied voltage. The data are consistent with the conclusion that the dominant excitation mechanism in GaN:Tm electroluminescent films is direct impact excitation of  $\text{Tm}^{3+}$  luminescent centers by hot electrons.

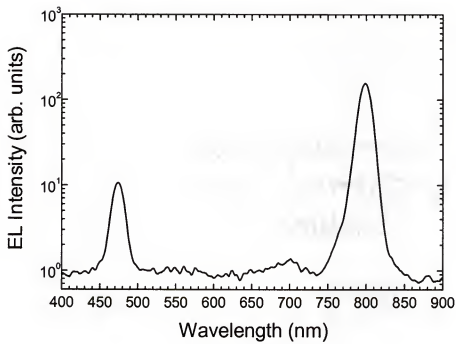


Figure 7-1. An alternating-current electroluminescent spectrum collected from a SD GaN:Tm ACTFEL device operating at room temperature.

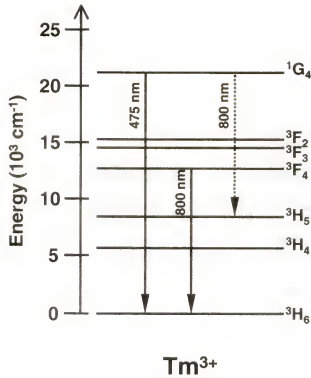


Figure 7-2 Simplified energy level diagram for a  $\text{Tm}^{3+}$  ion [52]. The radiative transitions corresponding to the blue and near-infrared emission peaks observed in the present work are also denoted in the figure. The multiplet labeled as  $^3\text{F}_4$  can be also referred to as  $^3\text{H}_4$  (and vice versa).



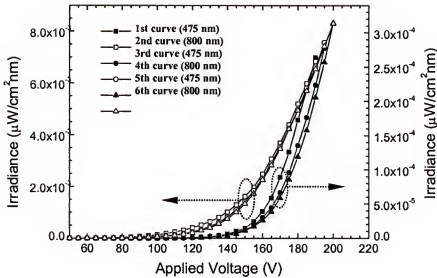


Figure 7-3. EL emission intensity versus applied AC peak voltage ( $I$ - $V$ ) curves. The 1st, 3rd, and 5th curves are sequentially collected for blue 475 nm emission. The 2nd, 4th, and 6th curves are sequentially collected for NIR 800 nm emission. Note the larger slope ( $dI/dV$ ) and larger threshold voltage,  $V_{th}$ , for the blue emission than those for NIR emission. Note the shift to higher threshold voltages for curves with higher numbers.

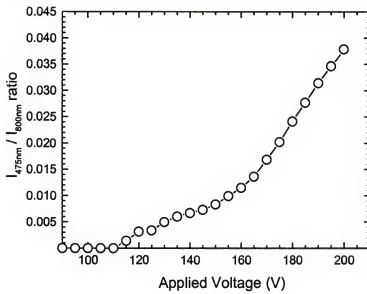


Figure 7-4. The dependence of the EL intensity ratio of 475 nm to 800 nm emission,  $I_{475}/I_{800}$ , on the AC voltage applied to the devices.

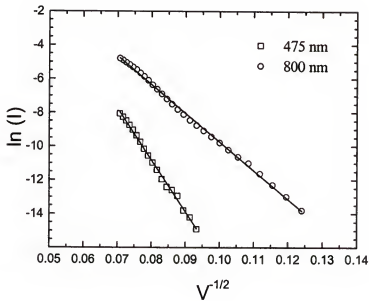


Figure 7-5. Plots of logarithm of the EL emission intensity,  $\ln(I)$ , versus the reciprocal square root of the applied AC voltage,  $V^{-1/2}$ , for blue 475 nm and NIR 800 nm emission peaks. Note that both emissions show a linear relationship between these parameters consistent with an impact excitation mechanism.

## CHAPTER 8 ELECTROLUMINESCENT CHARACTERISTICS AND STRUCTURAL PROPERTIES OF ERBIUM-DOPED GALLIUM NITRIDE

### 8.1 Introduction

Erbium (Er), one of lanthanides, has been an essential ingredient in optical fiber telecommunications technology. The electrons in the partially-filled  $4f^{11}$  inner shell of the trivalent Er ion are shielded from its surroundings by the electrons in the completely-filled  $5s^2$  and  $5p^6$  outer shells. Thus, the  $4f^{11}$  electrons do not play a role in the chemical bonding between the  $\text{Er}^{3+}$  ion and the surrounding ligands, and therefore, experience a weak electron-phonon coupling. This gives rise to optical emission peaks which are relatively insensitive to the host lattice and are determined by the energy of the transition between the  $4f^{11}$  levels of the  $\text{Er}^{3+}$  ions. The  $\text{Er}^{3+} 4f-4f$  intrashell transition from the first excited state ( $^4I_{13/2}$ ) to the ground state ( $^4I_{15/2}$ ) is of particular interest for the development of near-infrared (NIR) amplifiers and sources in optical fiber telecommunications technology. This is due to the fact that the  $^4I_{13/2} \rightarrow ^4I_{15/2}$  transition leads to the optical emission near  $1.54 \mu\text{m}$ , which coincides well with the wavelength of the minima in transmission loss and dispersion within silica-based optical fibers [19].

Silicon (Si) has been intensively examined as a host semiconductor for Er doping because of its predominance in the microelectronic applications [20]. However, Er-doped Si suffers from the strong temperature-induced quenching of the  $\text{Er}^{3+}$ -related luminescence efficiency. The relatively low solubility limit of Er in Si also hinders the employment of Er-doped Si in practical applications. Favenne *et al.* [56] suggested that

the thermal quenching of  $^4I_{13/2} \rightarrow ^4I_{15/2}$  intra-4f shell 1.54  $\mu\text{m}$  photoluminescence from  $\text{Er}^{3+}$  ions was less severe for the wider bandgap host semiconductors. This sparked a great deal of studies exploring a variety of wide bandgap semiconductors as a host material for Er doping. Among them, particular emphasis has been placed on GaN because of its unique properties such as a direct bandgap (3.4 eV at room temperature), good chemical and thermal robustness, excellent high-field transport properties, and relatively high Er solubility [19-21].

Besides the 1.54  $\mu\text{m}$  NIR emission, in the last few years, Er-doped GaN has also been shown to emit photons at visible wavelengths attributed to the  $\text{Er}^{3+}$  intrashell transitions from higher-lying 4f energy states. Several research groups have reported the strong visible photoluminescence (PL), cathodoluminescence (CL), and electroluminescence (EL) emission from Er-doped GaN near 530 and 550 nm, which correspond to the  $^4S_{3/2} \rightarrow ^4I_{15/2}$  and  $^4F_{9/2} \rightarrow ^4I_{15/2}$  radiative transitions in  $\text{Er}^{3+}$  ion, respectively. [19,48] Steckl and co-workers developed green-emitting electroluminescent devices (ELDs) based on Er-doped GaN and demonstrated the potential of Er-doped GaN for applications in flat-panel information displays [19].

Sputter deposition (SD) has been used to grow Er-doped GaN films by a few researchers. [22,23] SD technique offers low-cost mass-production benefits, which makes it possible to fabricate large-scale EL devices based on Er-doped GaN systems. In this section, electroluminescent characteristics and structural properties of SD-grown Er-doped GaN are studied as a function of Er concentration in GaN host films. The experimental procedure for sputter deposition of GaN thin films has been given in Section 3.1.

## 8.2 Experimental Results and Discussion

### 8.2.1 Crystalline Structure of Er-doped GaN

Figure 8-1 shows the  $\theta$ - $2\theta$  x-ray diffraction patterns obtained from the GaN:Er films grown on ATO/ITO/glass substrates with the variation of Er duty cycles from 0 % to 100 %. For comparison, the XRD pattern of a bare ATO/ITO/glass substrate is also presented in this figure. All the films were prepared under the same growth conditions except the duty cycle delivered to a Er target. As can be noticed, the three diffraction peaks observed from all the films at around  $30.5^\circ$ ,  $35.4^\circ$ , and  $37.6^\circ$  originate from the (222), (400), and (411) planes of the sputter-deposited ITO layer underlying beneath the  $\text{Al}_2\text{O}_3$ - $\text{TiO}_2$  dielectric layer grown by atomic layer deposition. No diffraction peak was observed from the  $\text{Al}_2\text{O}_3$ - $\text{TiO}_2$  dielectric layer since it has an amorphous structure. According to the Joint Committee on Powder Diffraction Standards (JCPDS) card, [33] the Bragg diffraction peaks at  $\sim 34^\circ$  and  $\sim 37^\circ$  are accounted for by diffraction from the (0002) and  $(10\bar{1}1)$  planes of wurtzite GaN phase. No extraneous peaks corresponding to any secondary phases, for example, Er-N or Er-Ga compounds were observed. It can be noticed that the Er-doped GaN films have a hexagonal wurtzite GaN structure with the strong preferential orientation in the [0001] direction perpendicular to the film surface.

Erbium doping did not introduce any detectable impurity phases but was found to affect the crystal structure quality of GaN host. As can be seen in Figure 8-1, the positions of both the GaN-related (0002) and  $(10\bar{1}1)$  Bragg diffraction peaks shift to lower  $2\theta$  values as the Er concentration is raised from 0 to 5 at.% while the positions of the (222), (400), and (411) diffraction peaks originating from the ITO film layer remains constant. This indicates that the interplanar distance  $d_{0002}$  ( $d$  spacing) in GaN expands as

the Er concentration in GaN host films is increased. The (0002) peak position was used as an input to determine the lattice constant,  $c$  of the wurtzite GaN. As shown in Figure 2(a), in the case of an undoped GaN film, the lattice constant,  $c$  was calculated to be 5.182 Å which is comparable to the reported values for bulk wurtzite GaN ( $c_o = 5.185$  Å). As the Er concentration is increased from 0 to 5 at.%, the lattice constant,  $c$  was increased. Since  $\text{Er}^{3+}$  ion has a larger ionic radius (0.96 Å) than  $\text{Ga}^{3+}$  ion (0.62 Å), [57] Er doping appears to induce the strain in GaN host lattice. And also, as presented in Figure 2(b), full width at half maximum (FWHM) of the wurtzite GaN (0002) diffraction peak was increased as the Er concentration is increased from 0 to 5 at.%. The (0002) peak broadening is considered to be due to the lattice strain induced by Er doping. However, according to the Scherrer's equation [27] where a larger FWHM of the XRD peak results from a smaller grain size, the (0002) peak broadening is likely due in part to a reduction in grain size. Although it is difficult to determine the relative effects of these two factors, grain size and microstrain factors, on the XRD (0002) peak broadening, the results obtained clearly indicate that the Er doping deteriorates the crystal structure quality of GaN host.

### 8.2.2 Visible and Near-Infrared Electroluminescence

The electroluminescence spectroscopic investigations from the Er-doped GaN ACTFEL devices were performed at room temperature for the visible and near-infrared (NIR) emissions in the 350 – 800 nm and 800 – 1800 nm wavelength ranges, respectively. Typical visible emission spectrum emitted from the Er-doped GaN films is shown in figure 8-3. The spectra show strong visible emissions originating from  $\text{Er}^{3+} 4f-4f$  intrashell transitions without any background emission attributed to the GaN host. We observed three visible emission peaks centered at around 530, 550, and 665 nm. From the

energy levels scheme of  $\text{Er}^{3+}$  ion as illustrated in figure 8-4, it can be found that the 530, 550, and 665 nm emissions correspond to the  $\text{Er}^{3+} 4f-4f$  intrashell transitions from  $^2H_{11/2}$ ,  $^4S_{3/2}$ , and  $^4F_{9/2}$  excited-state levels to the  $^4I_{15/2}$  ground-state [13], respectively. Similar room temperature visible EL spectra were reported earlier from Er-doped GaN grown by molecular beam epitaxy (MBE) [19]. This may suggest that SD- and MBE-grown GaN:Er films may qualitatively show similar luminescent properties. However there is a significant difference in terms of sharpness and relative intensities of emission peaks, which is considered to be due to a difference in crystal structure quality between the GaN:Er films grown by SD and MBE. It is well known that although the energy levels of the  $\text{Er}^{3+}$ -related optical transitions are little affected by the chemical environment around the  $\text{Er}^{3+}$  ions, the shape of the emission spectrum is strongly affected. Since our SD-grown GaN:Er films are polycrystalline, the crystalline surrounding of  $\text{Er}^{3+}$  ions is not defined as well as in MBE-grown single-crystalline GaN:Er. Thus, the luminescence lines from our SD-grown GaN:Er films are typically featureless and broad.

In Figure 8-5, typical NIR emission spectra measured at room temperature from the GaN:Er ACTFEL devices with increasing the voltage is presented. A strong NIR emission peak at around 1550 nm can be seen in the spectra, which can be assigned to the  $\text{Er}^{3+} 4f-4f$  intrashell transitions from the  $^4I_{13/2}$  excited-state levels to the  $^4I_{15/2}$  ground-state level [13], as depicted in Figure 8-4. The relatively weak NIR peak at 1000 nm arising from the  $\text{Er}^{3+} ^4I_{11/2} \rightarrow ^4I_{15/2}$  transition can be more clearly seen in the inset of Figure 8-5, which is an enlargement of the spectrum in the range from 800 to 1200 nm. Note that a shoulder on the higher wavelength side of 1550 nm emission peak is detected.



This presumably results from the Stark sub-level splitting of the  $\text{Er}^{3+}$  levels. These visible and near-infrared EL emission spectral features clearly demonstrate that the Er atoms incorporated in the GaN host were optically active in the form of trivalent ions.

### 8.2.3 Emission Intensity versus Voltage Analysis

Figure 8-6 shows the dependence of the EL intensities,  $I$ , of the 530 and 1550 nm emission peaks as a function of the AC peak voltages,  $V$ , applied to the devices. The  $I$ - $V$  data indicate that the intensities of both the 530 and 1550 nm emission peaks are increased as the AC voltage is raised above a threshold voltage. The threshold voltage,  $V_{th}$ , is typically defined as the voltage intercept of the extrapolation of the maximum slope of the  $I$ - $V$  curve back to zero intensity. The  $I$ - $V$  curves measured for 530 nm had a threshold voltage,  $V_{th}$ , of  $\sim 155$  V, but the 1500 nm emission showed a lower threshold voltage of  $\sim 140$  V. Since the excited-state energy level ( $^4S_{3/2}$ ) responsible for 530 nm is located above the  $^4I_{13/2}$  level corresponding to 1550 emission as depicted in figure 8-3, it can be speculated that the higher impact energy is needed to impact-excite the  $\text{Er}^{3+}$  ions into the higher excited-state  $^4S_{3/2}$  energy level. This result is consistent with the observations of other thin-film EL phosphor systems that are dominated by direct impact excitation processes by hot electrons.

Figures 8-7(a) and 8-7(b) show the variation of EL intensities for 530 nm and 1550 nm emission peaks, respectively, which were measured at 30 volts above the threshold voltage,  $I_{30}$ , as a function of the Er concentration in GaN host films. Both intensities sharply increase and then reach a maximum at an Er concentration of  $\sim 1$  at.%. Above this value, both EL intensities are decreased. The existence of an optimum EL

intensity can be explained by a concentration quenching of the luminescence of  $\text{Er}^{3+}$  ions at its high concentration via cross relaxation between adjacent  $\text{Er}^{3+}$  ions and/or energy transfer from  $\text{Er}^{3+}$  ions to non-radiative centers such as impurities, defects, and grain boundaries. As discussed above, the Er doping deteriorates the crystal structure quality of GaN host, resulting from the larger ionic radius of  $\text{Er}^{3+}$  than that of  $\text{Ga}^{3+}$ . This might also lead to a decrease in EL intensity at high Er concentration.

### 8.3 Summary

In this section, the electroluminescent characteristics and structural properties of Er-doped GaN thin films were studied as a function of the Er concentration. Er-doped GaN films were prepared by radio frequency (RF) planar magnetron co-sputtering of separate GaN and metallic Er targets in a pure nitrogen atmosphere. X-ray diffraction  $\theta$ - $2\theta$  scans revealed that the deposited GaN films possess a hexagonal wurtzite crystal structure, highly textured with a preferred orientation in the [0001] direction perpendicular to the surface of the film. As the Er concentration in GaN host films was increased from 0 to 5 at.%, full width at half maximum (FWHM) of the GaN (0002) Bragg diffraction peak and the  $c$  lattice constant were both increased. This presumably resulted from the micro-strain induced by the incorporation of larger Er atoms into GaN host. Alternating-current thin-film electroluminescence (ACTFEL) devices based on GaN:Er were fabricated using a standard half-stack configuration with a single bottom dielectric layer. We observed the  $\text{Er}^{3+}$ -related visible and near-infrared (NIR) electroluminescence from the fabricated devices operating at room temperature near 530, 550, 662, 1000, and 1550 nm, resulting from the  $\text{Er}^{3+}$   $4f-4f$  intrashell transitions from

the  $^2H_{11/2}$ ,  $^4S_{3/2}$ ,  $^4F_{9/2}$ ,  $^4I_{11/2}$ , and  $^4I_{13/2}$  excited-states to the  $^4I_{15/2}$  ground-state, respectively.

The optimum concentration of Er was determined to be around 1 at.% for both of the green 530 nm and NIR 1550 nm emission. Above 1 at.%, concentration quenching occurred.

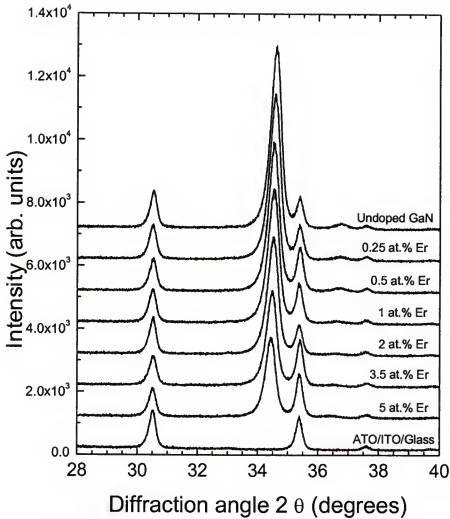


Figure 8-1. X-ray diffraction patterns obtained from Er-doped GaN films with the variation of Er concentration.

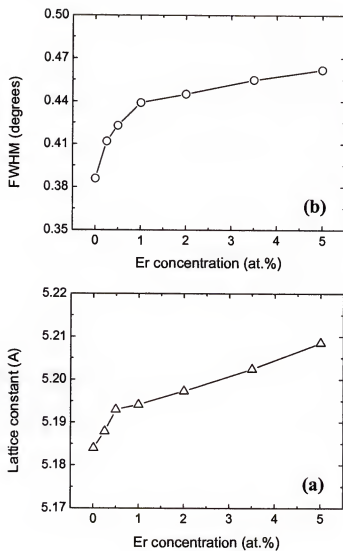


Figure 8-2. Variation in (a)  $c$  lattice constant of wurtzite GaN and (b) full width at half maximum (FWHM) of the (0002) wurtzite GaN peak as a function of Er concentration.

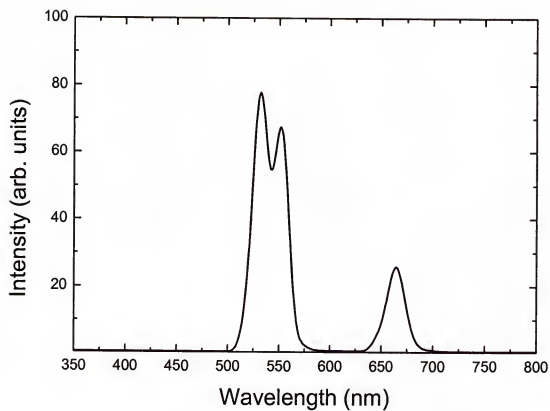


Figure 8-3. A typical room temperature visible spectrum emitted from the sputter-grown GaN:Er ACTFEL devices.

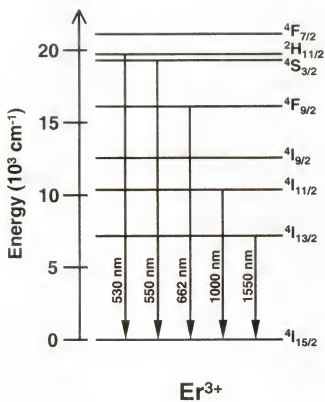


Figure 8-4. Energy level diagram for  $\text{Er}^{3+}$  ion emitting in the visible and near-infrared spectral regions [13].

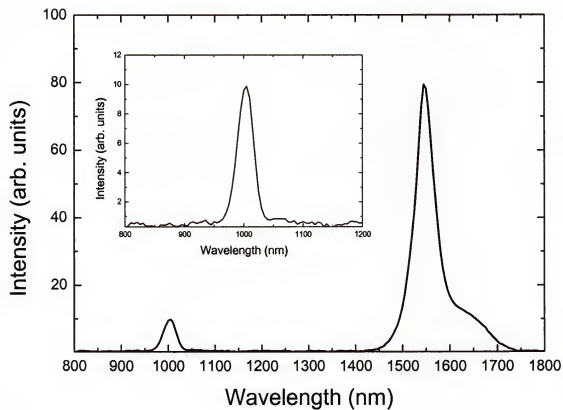


Figure 8-5. A typical room temperature near-infrared (NIR) spectrum emitted from the sputter-grown GaN:Er ACTFEL devices, showing 1000 and 1550 nm emissions.



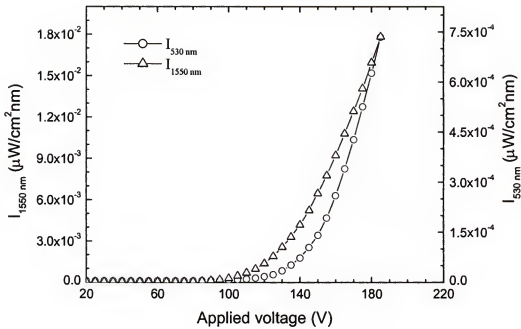


Figure 8-6. EL intensity versus applied AC peak voltage ( $I$ - $V$ ) data measured for peaks at the visible 532 and near-infrared 1550 nm from Er-doped GaN films.

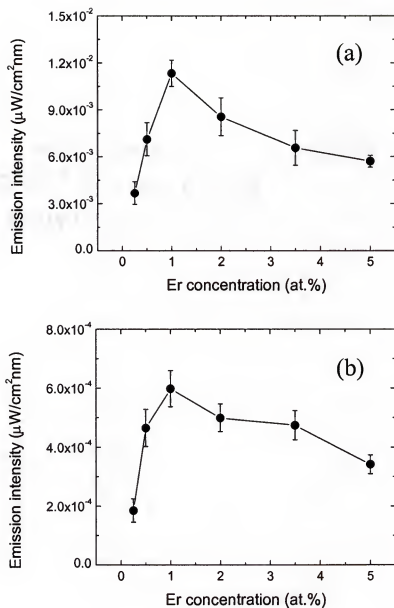


Figure 8-7. Variation in the (a) near-infrared 1550 nm and (b) visible 530 nm EL emission intensity, measured at 30 volts above a threshold voltage, as a function of Er concentration.

## CHAPTER 9

### NEAR-INFRARED ELECTROLUMINESCENCE FROM NEODYMIUM-DOPED GALLIUM NITRIDE

#### 9.1 Introduction

Over the past few years, rare earth (RE) impurity-based luminescence from GaN thin films has been the focus of great research interest. The majority of work to date has paid attention to RE-doped GaN systems emitting in visible spectral ranges owing to their potential applications in full-color flat-panel displays [19,48]. RE-doped GaN also has considerable potential for emission in near-infrared (NIR) spectral regions, particularly in connection with optical fiber telecommunications. Trivalent erbium ( $\text{Er}^{3+}$ ) ion is of particular interest because it is well known for its characteristic NIR emission at 1.55  $\mu\text{m}$ , which corresponds to the minimum transmission loss within standard silica-based glass fibers [20]. Very recently, room-temperature 1550 nm electroluminescence (EL) emission from Er-doped GaN films has been demonstrated by us and other groups [19], showing that it could be possible to fabricate NIR light-emitting EL devices based on RE-doped GaN systems.

Trivalent neodymium ( $\text{Nd}^{3+}$ ) ion is also an important ingredient in optical fiber telecommunication systems since its intra-4f-shell transitions lead to characteristic emission in NIR spectral ranges, particularly at 1.34  $\mu\text{m}$ , which is coincident with the low dispersion window of telecommunication fibers [58]. In addition, 1.06  $\mu\text{m}$  NIR light-emitting  $\text{Nd}^{3+}$ -doped lasers are very well established for operating with four-energy-level scheme with a narrow lasing linewidth [59]. Thus, the Nd ion could be suitable for use in

NIR light-emitting EL devices based on RE-doped GaN systems. However, the luminescence of Nd-doped GaN has not been studied to date, except one paper by Kim *et al.* [60] in which the photoluminescence (PL) investigation carried out at 6 K is presented. Here we report on a demonstration of near-infrared electroluminescent light emission at room temperature from Nd-doped GaN thin films. The experimental procedure for sputter deposition of GaN thin films has been given in Section 3.1.

## 9.2 Experimental Results and Discussion

### 9.2.1 X-ray Diffraction Analysis

Figure 9-1 shows the  $\theta$ - $2\theta$  x-ray diffraction pattern of ~1.2 at.% Nd-doped GaN films deposited on ATO/ITO/Corning 7059 glass substrates. For comparison, the XRD pattern obtained from undoped GaN films is also presented in this figure. These XRD data reveal that both undoped and Nd-doped GaN films have a highly textured hexagonal wurtzite GaN crystal structure with the [0001] preferential orientation normal to the film surface. No extraneous peaks corresponding to any secondary phases, for example, Nd-N or Nd-Ga compounds were observed. The interplanar distance of the (0002) plane,  $d_{(0002)}$ , was derived from the Bragg diffraction angle of the wurtzite GaN (0002) peak. The  $d_{(0002)}$  for Nd-doped GaN films is 2.596 Å, which is slightly larger than that determined from undoped GaN films (2.592 Å). This is indicative of the expansion of the GaN host lattice by Nd doping. The full width at half maximum (FWHM) of the (0002) diffraction peak, measured from the undoped GaN, is 0.39°, which is increased to 0.42° for Nd-doped GaN. The broadened FWHM of the (0002) peak, together with the expansion of the GaN host lattice, by Nd doping presumably results from the micro-strain induced by Nd ions

incorporated into the GaN host, which is attributed to the larger ionic radius of  $\text{Nd}^{3+}$  (0.99 Å) than that of  $\text{Ga}^{3+}$  (0.62 Å) [57].

### 9.2.2 Near-Infrared Electroluminescent Emission from Nd-doped GaN

The near-infrared electroluminescence emission spectra from Nd-doped GaN EL devices were collected at room temperature over an 800 – 1600 nm wavelength range with a resolution of 2 nm. Figure 9-2 shows the NIR EL emission spectra consisting of two distinct NIR emission peaks at 905 and 1082 nm. Another less intense NIR peak at around 1364 nm can be more clearly seen in the inset of Figure 9-3, which is an enlargement of the spectrum in the range from 1200 to 1550 nm. The intensities of all the three NIR emission peaks were increased upon increasing the AC peak voltage applied to the devices. Neither emission wavelengths nor relative intensities of the peaks change with increasing the voltage. From the optical transition level diagram of the  $\text{Nd}^{3+}$  ion [13], as illustrated in Figure 9-3, the 905, 1082, and 1364 nm NIR EL emissions arise from the radiative relaxation of the  $^4F_{3/2}$  excited-state energy level to the  $^4I_{9/2}$ ,  $^4I_{11/2}$ , and  $^4I_{13/2}$  levels in  $\text{Nd}^{3+}$  ions, respectively. Note that the  $^4F_{3/2} \rightarrow ^4I_{11/2}$  transition is the strongest. These NIR EL spectral features clearly demonstrate that the Nd dopant-impurities are incorporated in the form of trivalent ions in the wurtzite GaN host lattice. Kim *et al.* [60] reported similar NIR photoluminescence (PL) emission spectra measured at low temperature of 6 K from Nd-implanted GaN films grown by metal-organic chemical-vapor deposition (MOCVD). While very sharply structured NIR PL emissions related to the Stark sub-levels were observed at 6 K from their Nd-implanted MOCVD-grown GaN, the NIR EL emission peaks from our sputter-grown Nd-doped GaN films are

featureless and broad, and the Stark sub-level splitting is not clear enough to be resolved. This is presumably due to the polycrystalline nature of the sputter-grown films as well as higher temperature of EL measurements.

### 9.2.3 Visible Electroluminescent Emission from Nd-doped GaN

Visible EL emission spectra from the Nd-doped GaN EL devices were collected over the 300 – 800 nm wavelength range with a resolution of 2 nm. As shown in Figure 9-4, the relatively weak visible emission was observed and the spectrum consisted of two distinguishable peaks at 535 and 605 nm. These originate from the  $\text{Nd}^{3+} 4f-4f$  intrashell transitions from the  $^4G_{7/2}$  and  $^4G_{5/2}$  excited-states to the  $^4I_{9/2}$  ground-state, respectively [13], as depicted in Figure 9-3.

### 9.2.4 Excitation Mechanisms

The NIR emission intensities of the 905, 1082, and 1364 nm peaks are plotted in Figure 9-5 as a function of the AC peak voltages applied to the devices. Upon raising the voltage above a threshold voltage the EL intensities of all the three NIR emission peaks sharply increased. The threshold voltage,  $V_{th}$ , is typically defined as the intercept of the extrapolation of the maximum slope of the I-V data back to zero intensity. Note that all the three NIR emissions have almost the same threshold voltage of  $\sim 150$  V. As discussed above, all the three NIR emission peaks at 905, 1082, and 1364 nm originate from the same excited-state energy level ( $^4F_{3/2}$ ). Thus, the energy of a hot electron necessary to impact-excite  $\text{Nd}^{3+}$  ground-state electrons would be the same for all the three NIR transitions. Since the average energy of hot electrons is expected to increase with the applied field, it is reasonable that all the three NIR emission would be observed at the

same electric field. The external power efficiency,  $\eta_{EL}$ , of the Nd-doped GaN NIR-emitting EL devices was determined by dividing the measured radiant flux (in watts) from the devices by the product of the current passing through the devices times the voltage applied to the devices [61]. The external power efficiency of the Nd-doped GaN TFEL devices was  $\sim 1 \times 10^{-5}$ , which was measured at 40 volts above the threshold voltage.

### 9.3 Summary

In summary, strong near-infrared (NIR) electroluminescence emission at room temperature from the Nd-doped GaN thin films has been demonstrated. The Nd-doped GaN films were grown by radio-frequency planar magnetron co-sputter deposition. The sputter-grown Nd-doped GaN films had a strongly *c*-axis-oriented wurtzite GaN crystal structure without presence of any secondary phases. The three distinct NIR emission peaks at 905, 1082, and 1364 nm were observed from the Nd-doped GaN EL devices, which were associated with the  $\text{Nd}^{3+}$  intra-4*f*-shell transitions from the  $^4F_{3/2}$  excited-state to  $^4I_{9/2}$ ,  $^4I_{11/2}$ , and  $^4I_{13/2}$  levels, respectively. The threshold voltage for all the three NIR emission was the almost same at  $\sim 150$  V, presumably due to the excited-state energy level responsible for all the three NIR transitions being identical. Our results have shown the potential for developing near-infrared electroluminescent light-emitting planar optical sources based on GaN doped with Nd.

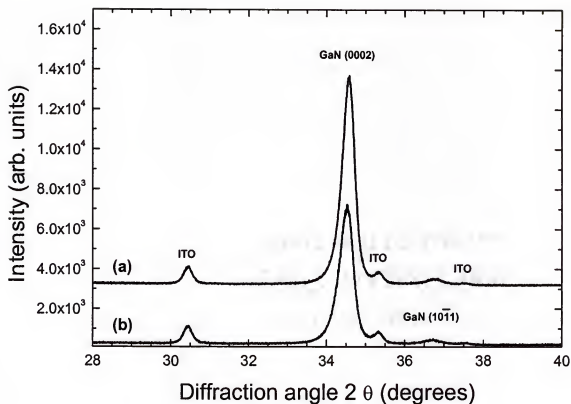


Figure 9-1. X-ray diffraction patterns collected from (a) undoped GaN and (b) ~1.2 at.% Nd-doped GaN films, both grown on  $\text{Al}_2\text{O}_3$ - $\text{TiO}_2$ /indium-tin-oxide/Corning 7059 glass substrates.



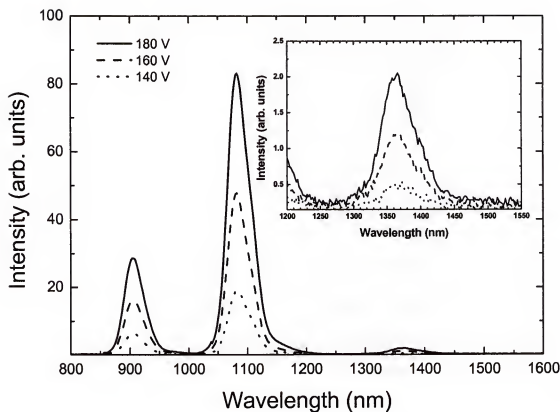


Figure 9-2. Near-infrared electroluminescence spectra emitted from Nd-doped GaN EL devices. The spectra were recorded at room temperature as a function of the AC peak voltage applied to the devices. Inset is an enlargement of the spectral region between 1200 and 1550 nm to show details of the lower intensity 1364 nm NIR emission peaks.

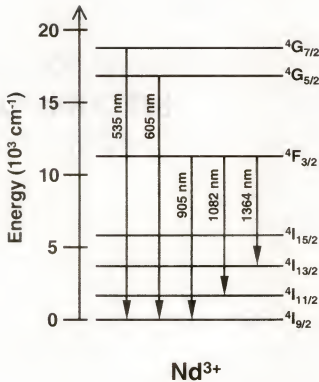


Figure 9-3. The optical transition level diagram of the trivalent Nd ion [13]. Arrows represent the radiative transitions corresponding to the visible and near-infrared electroluminescence emission peaks observed in the present work from Nd-doped GaN EL devices.

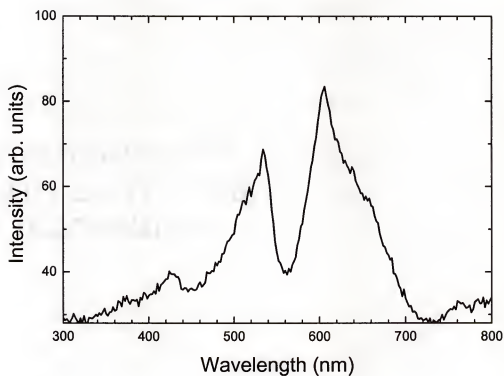


Figure 9-4. Visible electroluminescence emission spectrum emitted from Nd-doped GaN EL devices. The spectrum was recorded at room temperature with a resolution of 2 nm.

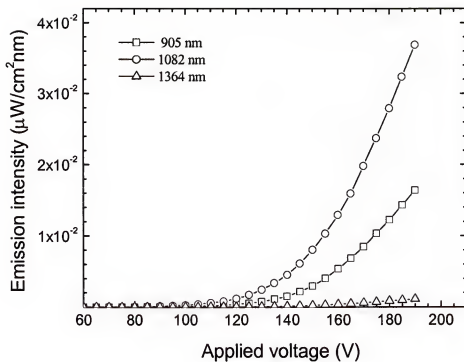


Figure 9-5. EL intensity versus applied AC peak voltage ( $I$ - $V$ ) curves collected for near-infrared emission peaks at 905, 1082, and 1364 nm.

## CHAPTER 10 CONCLUSIONS

Thin-film electroluminescent (TFEL) devices based on rare-earth-doped GaN systems, emitting photons at room temperature in both visible and near-infrared (NIR) spectral regions, were developed. The electroluminescent characteristics and excitation mechanisms of GaN doped with various rare earth species including europium (Eu), thulium (Tm), erbium (Er), and neodymium (Nd) have been studied.

The Eu-doped GaN exhibited the highest intensity photoluminescence emission peak in the red region at ~614 nm, resulting from the  $^5D_0 \rightarrow ^7F_2$  hypersensitive electric-dipole transition in the trivalent Eu ions. The optimum concentration of Eu for PL was approximately 1.8 at.%. The EL spectra consist of a series of well resolved emission peaks in the region of 530 – 700 nm, which originate from the  $^5D_J \rightarrow ^7F_{J'}$  ( $J = 0, 1; J' = 1, 2, 3, 4$ ) transitions. Higher EL voltage was needed to excite  $\text{Eu}^{3+}$  ions into the higher-lying  $^5D_1$  state versus the lower-lying  $^5D_0$  state, consistent with EL excitation being dominated by direct impact by hot electrons.

Visible and near-infrared EL emissions were demonstrated from GaN thin films doped with the trivalent Tm ions. The blue and NIR emission peaks at ~475 and ~800 nm were due to the  $\text{Tm}^{3+} 4f-4f$  intrashell transitions from the  $^1G_4$  or  $^3F_4$  excited-states to the  $^3H_6$  ground-state, respectively. The threshold voltage for 475 nm blue emission was consistently higher than that for 800 nm NIR emission. Also, the emission intensity ratio of 475 nm to 800 nm peaks was significantly increased with an increase in the applied

AC peak voltage. These data strongly indicate that the dominant excitation mechanism in Tm-doped GaN is direct impact excitation of  $\text{Tm}^{3+}$  by hot electrons.

Electroluminescent characteristics and structural properties of Er-doped GaN were investigated as a function of the Er concentration. X-ray diffraction data showed that the Er-doped GaN films have a highly textured wurtzite structure with the  $c$ -axis normal to the surface of the film. Visible and near-infrared EL emission peaks were observed from the Er-doped GaN EL devices at 530, 550, 660, 1000, and 1550 nm. These emissions were attributed to the  $\text{Er}^{3+} 4f-4f$  intrashell transitions from the  $^2H_{11/2}$ ,  $^4S_{3/2}$ ,  $^4F_{9/2}$ ,  $^4I_{11/2}$ , and  $^4I_{13/2}$  excited-state levels to the  $^4I_{15/2}$  ground-state, respectively. Full width at half maximum (FWHM) of the (0002) wurtzite-GaN diffraction peak and the lattice constant,  $c$ , both increased as the Er concentration was varied from 0 to 5 at.%, indicating that incorporation of larger Er atoms into GaN host expands the host lattice. The optimum concentration of Er was determined to be around 1 at.% for both of the green 530 nm and NIR 1550 nm emissions.

Strong near-infrared electroluminescent light emission was observed from the Nd-doped GaN EL devices. The three distinct NIR emission peaks were detected at 905, 1082, and 1364 nm, which were associated with the  $\text{Nd}^{3+}$  intra- $4f$ -shell transitions from the  $^4F_{3/2}$  excited-state to  $^4I_{9/2}$ ,  $^4I_{11/2}$ , and  $^4I_{13/2}$  levels, respectively. The threshold voltage for all the three NIR emission was the almost same at  $\sim 150$  V, presumably due to the excited-state energy level responsible for all the three NIR transitions being identical.

Visible and near-infrared electroluminescence emission from RE-doped GaN is a strong function of the film's structure and properties, therefore the effects of energetic particle bombardment on the deposited GaN host films have been investigated. A phase

transition at room temperature from the thermodynamically stable wurtzite to the metastable zinc-blende structure was observed in GaN films, resulting from increasing the impact energy of the hyperthermal species. The switching over from wurtzite GaN to zinc-blende GaN occurred at a compressive internal stress of around 1 GPa. The internal compressive stress above this threshold value apparently drives the GaN material into a high-pressure regime in the phase diagram where the zinc-blende phase is stable. It was also found that the energetic particle bombardment of the GaN films yielded a densely-packed microstructure with extremely smooth surface morphology. The high density results from porosity annihilation by knock-on processes and bombardment-induced adatom mobility.

Texture and properties of cubic GaN films were examined as a function of the film growth rate. X-ray diffraction  $\theta$ - $2\theta$  and pole-figure data showed that the cubic GaN films possess a textured structure with (111) crystallographic planes preferentially oriented parallel to the surface. The  $a$  lattice parameter of the cubic GaN was determined to be 4.59 Å. X-ray rocking curve analysis showed that the degree of [111] preferred orientation is higher for the GaN films grown at lower growth rates ( $\sim 16$  Å/min). Higher concentration of oxygen impurity, estimated to be  $\sim 3$  at.%, was present in the GaN films grown at these slow growth rates. Auger depth profiles indicated that the oxygen impurity was incorporated into the GaN films during growth rather than diffusing into the films after the growth or adsorbing during the AES analysis.

## CHAPTER 11 FUTURE WORK

Much work can still be done in this area of rare-earth-doped GaN. A few specific ideas related to the presented work are listed below:

- (1) Since the glass substrates were used in this study, the post-deposition annealing temperature was limited only up to 700 °C. It would be interesting to observe how the luminescent characteristics change with further increase of annealing temperature. The glass-ceramic plate may be used as a substrate for higher temperature annealing study.
- (2) Electroluminescence excitation mechanisms of rare-earth-doped GaN can be studied in detail by means of electrical characterization, such as charge versus voltage and capacitance versus voltage.
- (3) The dielectric material, which was used in this study, was alumina-titania. Since the electroluminescence intensity is a strong function of the interfacial properties between the dielectric and rare-earth-doped GaN, it would be interesting to observe how the electroluminescent characteristics change with changes with the dielectric materials. Tantalum oxide and silicon nitride would be potential candidates. Thickness of the dielectric layer can also be changed.
- (4) The luminescent characteristics of rare-earth-doped semiconductors are typically affected by the measurement temperature. Thus, it would be interesting to see how the luminescence changes with varying the temperature during the measurements.



(5) Blue, green, and red electroluminescent emissions were achieved from this study by the trivalent Tm, Er, and Eu ions. If these elements are co-doped into GaN host, various emission colors, such as orange, could be realized.

## LIST OF REFERENCES

1. Y. A. Ono, *Electroluminescent Displays*, Series on Information Display – Vol. 1 (World Scientific, Singapore, New Jersey, London, Hong Kong, 1995).
2. M. T. Anderson, R. J. Walko, M. L. F. Phillips, Mater. Res. Soc. Symp. **345**, 269 (1995).
3. P. D. Rack and P. H. Holloway, Mater. Sci. Eng. R **21**, 171 (1998).
4. S. S. Sun, E. Dickey, J. Kane, and P. N. Yocum, Proc. 17<sup>th</sup> Int. Display Research Conf., 301 (1997).
5. W. A. Barrow, R. C. Coover, E. Dickey, C. N. King, C. Laakso, S. S. Sun, R. T. Tuenge, R. Wentross, and J. Kane, SID 93 Digest **24**, 761 (1993).
6. A. J. Steckl and R. Birkhahn, Appl. Phys. Lett. **73**, 1700 (1998).
7. J. Heikenfeld and A. J. Steckl, Appl. Phys. Lett. **77**, 3520 (2000).
8. K. Gurumurugan, H. Chen, G. R. Harp, W. M. Jadwisieniczak, and H. J. Lozykowski, Appl. Phys. Lett. **74**, 3008 (1999).
9. R. Mach and G. O. Mueller, Semicond. Sci. Technol. **6**, 305 (1991).
10. P. D. Keir, W. M. Ang, and J. F. Wager, SID 95 Digest, 476 (1995).
11. S. Shionoya and W. M. Yen, *Phosphor Handbook* (CRC Press, Boca Raton, FL, 1999).
12. G. Blasse and B. C. Grabmeier, *Luminescent Materials* (Springer-Verlag, New York, 1994).
13. G. H. Dieke, in *Spectra and Energy Levels of Rare Earth Ions in Crystals*, edited by H. M. Crosswhite and H. Crosswhite (Interscience Publishers, New York, 1968).
14. A. J. Freeman and R. E. Watson, Phys. Rev. **127**, 2058 (1962).
15. D. Kahng, Appl. Phys. Lett. **13**, 210 (1968).
16. W. A. Barrow, R. C. Coover, E. Dickey, C. N. King, C. Laakso, S. S. Sun, R. T. Tuenge, R. Wentross, and J. Kane, SID 93 Digest **24**, 761 (1993).

17. S. S. Sun, E. Dickey, J. Kane, and P. N. Yocum, Proc. 17<sup>th</sup> Int. Display Research Conf., p. 301 (1997).
18. Y. Nakanishi, T. Nakajima, H. Kominami, M. Ehara, and Y. Hatanaka, Phys. Status Solidi B, **229**, 1011 (2002).
19. A. J. Steckl, J. C. Heikenfeld, D. S. Lee, M. J. Garter, C. C. Baker, Y. Q. Wang, and R. Jones, IEEE J. Sel. Top. Quant. **8**, 749 (2002).
20. R. G. Wilson, R. N. Schwartz, C. R. Abernathy, S. J. Pearton, N. Newman, M. Rubin, T. Fu, and J. M. Zavada, Appl. Phys. Lett. **65**, 992 (1994).
21. H. J. Lozykowski, W. M. Jadwisieniczak, and I. Brown, Appl. Phys. Lett. **74**, 1129 (1999).
22. H. Chen, K. Gurumurugan, M. E. Kordesch, W. M. Jadwisieniczak, and H. J. Lozykowski, MRS Internet J. Nitride Semicond. Res. **5S1**, W3.16 (2000).
23. S. B. Aldabergenova, A. Osvet, G. Frank, H. P. Strunk, P. C. Taylor, and A. A. Andreev, J. Non-cryst. Solids **299-302**, 709 (2002).
24. S. J. Pearton, J. C. Zolper, R. J. Shul, and F. Ren, J. Appl. Phys. **86**, 1 (1999).
25. S. Strite and H. Morkoç, J. Vac. Sci. Technol. B **10**, 1237 (1992).
26. S. Nakamura, Science **281**, 956 (1998).
27. B. D. Cullity, *Elements of X-ray Diffraction*, 2nd ed. (Addison-Wesley, New York, 1978).
28. S. Wei, B. Li, T. Fujimoto, and I. Kojima, Phys. Rev. B **58**, 3605 (1998).
29. J. F. Wager and P. D. Keir, Ann. Rev. Mater. Sci. **27**, 223 (1997).
30. M. L. Reed, N. A. El-Masry, H. H. Stadelmaier, M. K. Ritums, M. J. Reed, C. A. Parker, J. C. Roberts, and S. M. Bedair, Appl. Phys. Lett. **79**, 3473 (2001).
31. T. Lei, M. Fanciulli, R. J. Molnar, T. D. Moustakas, R. J. Graham, and J. Scanlon, Appl. Phys. Lett. **59**, 944 (1991).
32. T. Dietl, H. Ohno, F. Matsukura, J. Cibert, and D. Ferrand, Science **287**, 1019 (2000).
33. Joint Committee on Powder Diffraction Standards (JCPDS), Powder Diffraction Files, Inorganic, No. 2-1078.
34. T. Kurobe, Y. Sekiguchi, J. Suda, M. Yoshimoto, and H. Matsunami, Appl. Phys. Lett. **73**, 2305 (1998).

35. J. H. Kim and P. H. Holloway, Appl. Phys. Lett., submitted, (2003).
36. J. H. Kim and K. W. Chung, J. Appl. Phys. **83**, 5831 (1998).
37. J. H. Kim and P. H. Holloway, J. Vac. Sci. Technol. A **20**, 928 (2002).
38. C. Weismantel, K. Bewilogua, D. Dietrich, H.-J. Erler, H.-J. Hinneberg, S. Klose, W. Nowick, and G. Reisse, Thin Solid Films **72**, 19 (1980).
39. I. W. Kim, Q. Li, L. D. Marks, and S. A. Barnett, Appl. Phys. Lett. **78**, 892 (2001).
40. J. H. Kim, D. H. Ahn, Y. H. Kim, and H. K. Baik, J. Appl. Phys. **82**, 658 (1997).
41. J. F. O'Hanlon, *A User's Guide to Vacuum Technology*, 2<sup>nd</sup> ed. (John Wiley & Sons, New York, 1989).
42. D. Chandrasekhar, D. J. Smith, S. Strite, M. E. Lin, and H. Morkoç, J. Cryst. Growth **152**, 135 (1995).
43. G. E. Muileberg, *Handbook of Auger Electron Spectroscopy* (Perkin-Elmer, Eden Prairie, MN, 1978).
44. R. S. Bhattacharya and P. H. Holloway, Appl. Phys. Lett. **38**, 545 (1981).
45. J. F. Moulder, W. F. Stickle, P. E. Sobol, and K. D. Bomben, *Handbook of X-ray Photoelectron Spectroscopy* (Physical Electronics, Inc., Eden Prairie, 1995).
46. R. Vercaemst, D. Poelman, L. Fiermans, R. L. V. Meirhaeghe, W. H. Laflère, and F. Cardon, J. Electron Spectrosc. **74**, 45 (1995).
47. S. A. Studenikin and M. Cocivera, Thin Solid Films **394**, 264 (2001).
48. H. J. Lozykowski, W. M. Jadwisieniczak, and I. Brown, J. Appl. Phys. **88**, 210 (2000).
49. R. D. Peacock, in *Structure and Bonding* Vol. 22, edited by J. D. Dunitz, P. Hemmerich, R. H. Holm, J. A. Ibers, C. K. Jorgensen, J. B. Neilands, D. Reinen, R. J. P. Williams, (Springer-Verlag, Berlin, 1975).
50. S. Morishima, T. Maruyama, and K. Akimoto, J. Cryst. Growth **209**, 378 (2000).
51. J. H. Kim, M. R. Davidson, and P. H. Holloway, Appl. Phys. Lett. **83**, 4746 (2003).
52. A. J. Steckl, M. Garter, D. S. Lee, J. Heikenfeld, and R. Birkhahn, Appl. Phys. Lett. **75**, 2184 (1999).
53. A. Kato, M. Katayama, A. Mizutani, N. Ito, and T. Hattori, J. Appl. Phys. **81**, 445 (1997).

- 54. A. K. Alshawwa and H. J. Lozykowski, J. Electrochem. Soc. **141**, 1070 (1994).
- 55. X.-Y. Jiang, Z.-L. Zhang, W.-M. Zhao, Z.-G. Lui, and S.-H. Xu, J. Phys.: Condens. Matter **6**, 3279 (1994).
- 56. P. N. Favennec, H. L'Haridon, M. Salvi, D. Moutonnet, and Y. Le Guillou, Electron Lett. **25**, 718 (1989).
- 57. H. J. Lozykowski, Phy. Rev. B **48**, 17758 (1993).
- 58. A. J. Steckl and J. M. Zavada, MRS Bull. **24**, 33 (1999).
- 59. F. T. Arecchi and E. O. Schulz-Dubois, *Laser Handbook* (North Holland, Amsterdam, 1972).
- 60. S. Kim, S. J. Rhee, X. Li, J. J. Coleman, and S. G. Bishop, Phys. Rev. B **57**, 14588 (1998).
- 61. X. Gage, D. Evans, M. Hodapp, H. Sorensen, K. Jamison, and B. Krause, *Optoelectronics/Fiber-Optics Applications Manual*, 2<sup>nd</sup> ed. (McGraw-Hill, New York, 1981).

## BIOGRAPHICAL SKETCH

Joo Han Kim was born in Seoul, South Korea, in June of 1969. He entered Yonsei University, also in Seoul, South Korea, in 1989 to study materials science and engineering. He earned his Bachelor of Science degree and continued at Yonsei University for his graduate study and obtained his Master of Science degree. The research area for his master's degree was the growth and characterization of semiconducting thin films. After graduation from Yonsei University, he started his professional carrier at LG Electronic Research Center, located in Seoul, South Korea. He worked as a research engineer and was involved in the development of electronic devices.

In 1999, he moved to the University of Florida to pursue his Ph.D. study in the Department of Materials Science and Engineering with a specialty of electronic materials. His main research area under the supervision of Professor Paul H. Holloway was the development of visible and near-infrared light-emitting thin-film electroluminescent devices based on gallium nitride doped with rare earth elements.

Mr. Kim received the "Korean Graduate Student Award and Scholarship" for best performance in Materials Science at UF in 2003. He also received the "Outstanding Graduate Research Award and Scholarship" from the American Vacuum Society in November 2003. He is now scheduled to start his professional carrier at Intel Corporation located in Portland, Oregon, as a Senior Research Engineer in January of 2004.

I certify that I have read this study and that in my opinion it conforms to acceptable standards of scholarly presentation and is fully adequate, in scope and quality, as a dissertation for the degree of Doctor of Philosophy.



Paul H. Holloway, Chairman  
Distinguished Professor of Materials  
Science and Engineering

I certify that I have read this study and that in my opinion it conforms to acceptable standards of scholarly presentation and is fully adequate, in scope and quality, as a dissertation for the degree of Doctor of Philosophy.



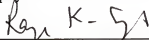
Stephen J. Pearton  
Distinguished Professor of Materials  
Science and Engineering

I certify that I have read this study and that in my opinion it conforms to acceptable standards of scholarly presentation and is fully adequate, in scope and quality, as a dissertation for the degree of Doctor of Philosophy.



Timothy J. Anderson  
Professor of Chemical Engineering

I certify that I have read this study and that in my opinion it conforms to acceptable standards of scholarly presentation and is fully adequate, in scope and quality, as a dissertation for the degree of Doctor of Philosophy.



Rajiv K. Singh  
Professor of Materials Science and  
Engineering

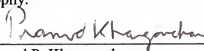
I certify that I have read this study and that in my opinion it conforms to acceptable standards of scholarly presentation and is fully adequate, in scope and quality, as a dissertation for the degree of Doctor of Philosophy.



Wolfgang Sigmund  
Associate Professor of Materials Science  
and Engineering

This dissertation was submitted to the Graduate Faculty of the College of Engineering and to the Graduate School and was accepted as partial fulfillment of the requirements for the degree of Doctor of Philosophy.

December, 2003



---

Pramod P. Khargonekar  
Dean, College of Engineering

---

Winfred M. Phillips  
Dean, Graduate School